American Mineralogist, Volume 110, pages 1898–1918, 2025

Pre-eruptive characteristics of "suspect" silicic magmas in Carlin-type Au-forming systems

Celestine N. Mercer[1,*], Julie Roberge[2,†], Regina M. Khoury[1,‡], and Albert. H. Hofstra[1]

[1]U.S. Geological Survey, Geology, Geophysics & Geochemistry Science Center, Denver Federal Center, Box 25046, MS-973, Denver, Colorado 80225, U.S.A.
[2]Instituto Politécnico Nacional (IPN), Escuela Superior de Ingeniería y Arquitectura (ESIA), Unidad Ticomán, Calz. Ticomán 600, Delg. Gustavo A. Madero, C.P. 07340, Ciudad de México (CDMX), Mexico

Abstract

World-class Carlin-type Au deposits hosted in sedimentary rock were formed when profuse Eocene silicic magmatism swept across northern Nevada in response to arc migration. Carlin-type Au deposits formed along with porphyry/skarn Cu-Mo-W-Au deposits, epithermal Ag-Au deposits, and distal disseminated Ag-Au deposits. But unlike these other Au-bearing deposits that have clear associations with igneous intrusions, Carlin-type ore deposits appear to have formed distant from concealed plutons, and their origin remains controversial. Despite decades of abundant geophysical, geochronological, and geochemical studies suggesting the involvement of magmas, concrete evidence for magmatic involvement is still lacking. Consequently, the involvement of contemporaneous igneous systems remains inferred based on age, proximity, and variable isotopic, geochemical, and geophysical clues. A recent synthesis of deposit models postulates that Carlin-type Au deposits are intrusion-related, but that the causative magmas reside deeper (~6–12 km) than in typical porphyry and peripheral systems (~3–5 km), meaning that Carlin-type deposits are perhaps more distal expressions of igneous intrusions. We investigate a collection of "suspect" magmatic systems over a ~7 m.y. timespan (~41–34 Ma) that are contemporaneous with and near known Carlin-type ore deposits. We report results of a multifaceted array of in situ geochemical analyses (FTIR, EMP, SHRIMP-RG, LA-ICP-MS) of quartz-hosted melt inclusions, biotite, and quartz to better characterize the pre-eruptive characteristics of these magmas. We also report results of thermobarometry and thermodynamic phase equilibria modeling to help place constraints on magmatic reservoir depths and processes. Rather than a single "flavor" of silicic magma, we observe a surprisingly broad compositional spectrum of rhyolites, with one end of the spectrum exhibiting more arc-like (I-type) characteristics and the other end displaying more post-subduction, thick-crust extensional (A-type) characteristics. This broad compositional spectrum suggests a more complex picture of silicic crustal magmatism operating over a narrow span of time during slab rollback. Despite this spectrum, magmatic systems in this study are consistently ferroan and generally peraluminous, which we interpret as an expression of the relatively elevated geotherm at the time and incorporation of variable amounts of highly peraluminous metasedimentary crustal components. The silicic magma spectrum encompasses a range of mineralization associations, including subduction-related Cu-Mo-W-Au-Ag and post-subduction, thick-crust extensional rare-metal Mo-Sn-W-F-Be-Ag-Au, consistent with the prolific and diverse array of ore deposits that formed during this time. Carlin-type Au deposition appears to be associated with nearly the entire magmatic spectrum. This apparent indifference to silicic magma "flavor" would seem to imply that if magmas are involved in Carlin-type Au deposit genesis, they perhaps do not need to be compositionally specialized and/or possibly are only relevant as heat sources driving circulation to remobilize and redistribute metals.

Keywords: Carlin-type Au, rhyolite, melt inclusions, magma reservoirs, slab rollback, ignimbrite flare-up, ore deposits, Nevada

Introduction

Carlin-type ore-forming systems in Nevada contain one of the world's most conspicuous endowments of Au, estimated at ~7230 tonnes (~255 million ounces) (Muntean and Cline 2018). Their discovery led to a Au boom that launched the United States as one of the world's leading producers for 40 years running. These sedimentary rock-hosted disseminated Au deposits formed during a prolific, Eocene metallogenic episode in Nevada (Barton 1996; Hofstra and Wallace 2006; Best et al. 2016) that coincided with profuse volcanism due to middle Cenozoic arc migration (Humphreys 1995; Dickinson 2006). Carlin-type Au deposits formed along with other magmatic-hydrothermal ore deposits in the region, such as porphyry/skarn Cu-Mo-W-Au, epithermal Ag-Au deposits, and distal disseminated Ag-Au deposits. Unlike these other deposit types, however, Carlin-type Au deposits appear to have formed distant from concealed plutons and their origin remains controversial (i.e., magmatic-metamorphic-sedimentary) (Cline et al. 2005;

* Corresponding author E-mail: cmercer@usgs.gov Orcid https://orcid.org/0000-0001-8359-4147
† Orcid https://orcid.org/0000-0002-8293-6325
‡ Present address: CalPoly Humboldt, Department of Geology, 1 Harpst Street, Arcata, California 95521, U.S.A.

0003-004X/25/0012–1898$05.00/DOI: https://doi.org/10.2138/am-2024-9372

Emsbo et al. 2006; Large et al. 2011; Muntean et al. 2011; Large et al. 2016; Cline 2018). At the heart of the problem is the fact that despite decades of plentiful geophysical, geochronological, and geochemical studies suggesting the involvement of magmas (e.g., Barnes et al. 2001; John 2001; Ressel and Henry 2006; du Bray 2007; Ryskamp et al. 2008; Johnson et al. 2015; Watts et al. 2016, 2019; Henry et al. 2020, 2023), there is no direct field evidence of magmatic involvement that is commonly observed in porphyry and peripheral (skarn, epithermal, distal disseminated) deposits. The best preserved and documented example for such concrete field evidence is perhaps the Jurassic Yerington porphyry Cu district in Nevada, where one can trace the system from pluton to lithocap: starting from the top of the upper crustal Yerington batholith (~7 km paleodepth) to multiple cupolas (~4–5 km paleodepth) where dikes emanate and transition over ~4 to 1 km paleodepth to mineralized breccias, porphyry style Cu-Mo veins, Fe-oxide-Au-Cu mineralization, hornfels, Cu skarns, epithermal Au-Ag mineralization and quartz-alunite lithocaps (<1 km paleodepth); along with associated contact zones and alteration haloes that signify distinct thermal and fluid contributions from contemporaneous, persistent magmatic intrusions (e.g., Dilles et al. 2000; Sepp 2022; Castellanos-Melendez et al. 2024). Of the many Carlin-type Au deposits mined, the Cortez Hills Au deposit has some of the best documented field relationships for magmatic involvement. There, one can observe shallow dikes (~0–1 km from the current surface) of ore-forming age that crosscut Au ore, and vice versa (Arbonies et al. 2011; Henry et al. 2020), but no examples of magmatic features directly transitioning to alteration or ore features. This is somewhat expected because Carlin-type mineralization is characteristically low temperature (~180–240 °C), structurally controlled, and thought to form at relatively shallow depths (1–3 km), far from intrusions. While unsatisfyingly indirect, recent studies of melt inclusions trapped within those Cortez Hills dikes suggest contemporaneous magmas residing in polybaric magma reservoirs (~4–9 km depth) would have expelled fluids at depths starting at ~5 km and continuing to the surface, overlapping where Carlin-type mineralization occurred. However, it remains to be seen whether those fluids could have carried any ingredients crucial to ore formation (Mercer 2021).

With concrete field evidence decidedly still lacking, the involvement of contemporaneous igneous rocks remains inferred based on age, proximity, sporadic magmatic isotopic signatures, geochemical signatures in rare fluid inclusions, and geophysical clues (Hofstra et al. 1999; Hofstra and Cline 2000; Cline et al. 2005; Ressel and Henry 2006; Muntean et al. 2011; Johnson et al. 2015, 2020; Large et al. 2016; Cline 2018; Muntean 2018; Muntean and Cline 2018; Cousens et al. 2019; Henry et al. 2020, 2023; Hollingsworth 2022; Jin et al. 2020; Hofstra et al. in press). This has led researchers to postulate that Carlin-type Au deposits are intrusion-related, but that the causative magmas reside deeper (~6–12 km) (Muntean et al. 2011; Henry et al. 2020, 2023) than in typical porphyry and peripheral systems (~3–5 km) (Audétat and Simon 2012); i.e., Carlin-type deposits are perhaps a more distal expression of igneous intrusions. A recent synthesis of models by Muntean and Cline (2018) suggests that while Carlin-type Au deposits probably form by distinctive processes, there likely exists a spectrum of deposits with characteristics ranging between Carlin-type Au, distal disseminated deposits, and epithermal deposits, i.e., Carlin-type Au deposits may form by unique geological processes, but may be related to the same magmatic systems.

To better characterize the petrogenesis of "suspect" magmatic systems, we sampled a suite of igneous rocks contemporaneous with nearby Carlin-type Au deposits in northern Nevada (i.e., same age as mineralization within analytical error, between ~41–34 Ma; and within ~0–5 km of known deposits), staying away from skarn, epithermal, or distal disseminated deposits in the region. We report the results of in situ geochemical analyses (FTIR, EMP, SHRIMP-RG, LA-ICP-MS) of quartz-hosted melt inclusions (n = 237) as well as phenocrysts of biotite (n = 250) and quartz (n = 48) to help characterize the pre-eruptive characteristics of these magmas. In addition, we employ thermobarometry and modeling of thermodynamic phase equilibria to help provide context and better define the magma reservoir conditions (e.g., depth, fluid saturation depth), potentially contributing to Carlin-type Au system genesis.

Tectonic, Magmatic, and Metallogenic Framework of Northern Nevada

Northern Nevada lies within the northern Basin and Range Province of the western United States (Fig. 1). The evolutionary complexity of the region for over the last eon has produced one of the world's richest metallogenic provinces (e.g., Dickinson 2006; Hofstra and Wallace 2006; du Bray 2007; Best et al. 2016; Henry et al. 2020; John and Henry 2020). Lithospheric preconditioning likely played a key role in setting the stage for the prolific Eocene magmatism and metallogeny that occurred during the formation of Carlin-type Au deposits in northern Nevada.

Eocene Carlin-type Au deposits formed during a period of dynamically shifting subduction-related magmatism. As the previously shallowly subducting Farallon slab began to roll back beneath the region, upwelling asthenospheric mantle flowed into the formerly metasomatized lithospheric mantle wedge (Fig. 1) (Humphreys 1995; Dickinson 2006). This resulted in abundant melt generation by three mechanisms: (1) dehydration of the Farallon plate, inducing hydrous melting of the overlying mantle wedge; (2) dry, decompression melting of hot asthenospheric mantle due to mantle flow in the wedge; and (3) melting of lithospheric mantle by heat from upwelling asthenosphere or wedge-derived magmas. This produced an unusually hot deep-crustal thermal regime and led to the ignimbrite flare-up (Best et al. 2016). The thermal regime of the crust and tectonic stresses drive the evolution of deep crustal melt traps, interconnected crustal magma reservoirs, magma production rates, and mobilization of crystal mushes (e.g., Bachmann and Bergantz 2008; de Silva 2008; Loucks 2021). Ensuing magmas that swept southwestward across Nevada (Fig. 1; red dashed lines and shaded fields) were dominated by calc-alkaline, moderately oxidized, rhyolitic, dacitic, and trachydacitic intrusions and ignimbrites, caldera complexes, and associated hydrothermal activity (Henry and John 2013; Best et al. 2016; Timmermans et al. 2020). While there are very few Eocene mafic rock units exposed, mafic magmatism likely played a key role in providing an exceptional amount of advective thermal energy in the deep- and mid-crust to generate

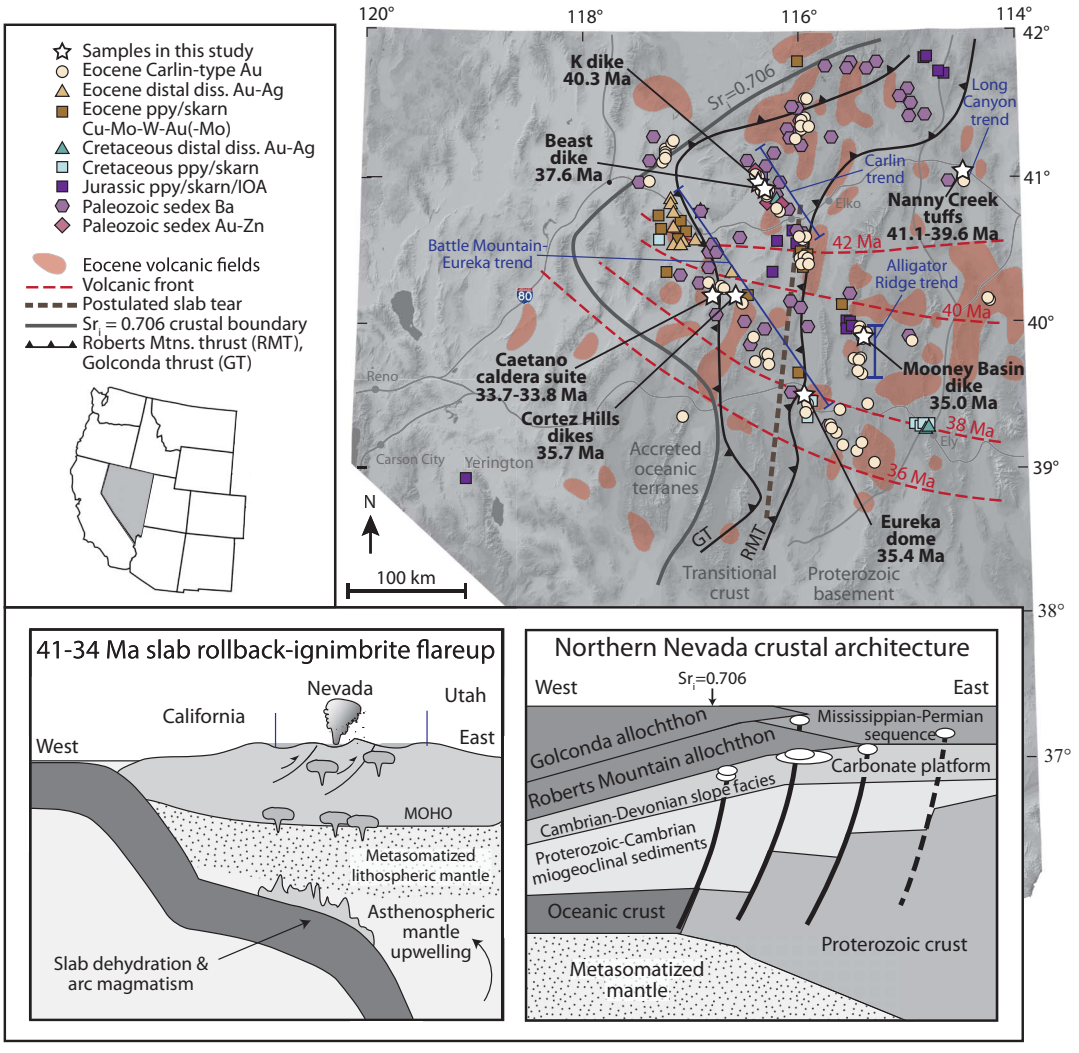

Figure 1. Map of Nevada, tectonic setting, and sampling sites. (**top**) Location of Eocene igneous samples from this study (white stars), Eocene volcanic fields (red fields) (Ryskamp et al. 2008) and fronts (red dashed lines) (Henry and John 2013), distribution of regional ore deposits (modified after Emsbo et al. 2006), major crustal features including Sri boundary delineating the edge of the craton and accreted terranes (gray line) (Tosdal et al. 2000), the Roberts Mountains and Golconda thrusts (RMT and GT; black saw-toothed lines) (Grauch et al. 2003), and the postulated slab tear (brown dashed line) (McQuarrie and Oskin 2010; Best et al. 2016). (**bottom, left**) Schematic east-west cross section of Nevada showing the tectonic setting during the Eocene (after Christiansen et al. 2007). (**bottom, right**) Schematic east-west cross section of northern Nevada showing the inferred lithospheric architecture including major basement faults, accreted terrains, and location of Carlin-type Au deposits (white ovals; modified after Emsbo et al. 2006). Ppy = porphyry; IOA = iron oxide apatite.

and sustain felsic magmatism. The Eocene magmatic systems traversed an unusually thick crust of the Nevadaplano (~40–70 km) (Best et al. 2009; Snee and Miller 2022). Crustal thickening was the product of several previous orogenies across the region (Late Devonian-Mississippian Antler, Permian-Triassic Sonoma, Jurassic-Cretaceous Sevier hinterland), punctuated by thrusting and accretion of deep-water oceanic strata (i.e., oceanic shales, siliciclastics, cherts, and basalts of the Roberts Mountains allochthon, Golconda allochthon) (Dickinson 2006; Jones Crafford 2008; Yonkee and Weil 2015; Holm-Denoma et al. 2017) over the Neoproterozoic to early Paleozoic passive margin miogeoclinal sediments and slope/shallow water carbonate platform. The Roberts Mountain and Golconda thrust faults bisect the study area (Fig. 1). Hence, ascending Eocene magmas traversed two lithospheric domains, with Proterozoic lithosphere to the east of the Sri = 0.706 line and accreted oceanic terranes to the west, with transitional lithosphere in between (Fig. 1, dark gray line) (Tosdal et al. 2000; Dickinson 2006; Best et al. 2016). Most Carlin-type Au deposits are hosted east of the Sri = 0.706 line in slope facies rocks near the carbonate platform margin (Fig. 1). Finally, middle Miocene bimodal volcanism and classic Basin and Range extension progressed, which thinned the crust to ~30 km and largely shaped northern Nevada as we see it today (Fig. 1) (Dickinson 2006; Colgan and Henry 2009).

At nearly all tectonic stages, mineralization occurred throughout the region. Anoxic conditions along the Neoproterozoic to early Paleozoic passive margin led to the formation of marine chemocline black shales enriched in Ni-V-Mo-Se-Hg-Re and REE-phosphorites along the ocean basin margins (Emsbo et al. 2015, 2016). Deep basement faults inherited during previous continental rifting helped to focus basin brines, forming Ordovician and Devonian sedimentary exhalative Au-Pb-Zn(Ag-Ba) deposits (Emsbo et al. 1999, 2006). Back arc magmatism associated with the Mesozoic Sierran arc further west produced localized base- and precious-metal mineralization, including Jurassic reduced intrusion-related Au deposits and iron oxide apatite deposits (with the aforementioned Yerington porphyry Cu district forming further west of the study area, Fig. 1), and Cretaceous porphyry Cu-Au, Mo-Cu, and distal disseminated Au-Ag deposits (Hofstra and Wallace 2006; Vikre et al. 2011). The same crustal-scale faults served to focus future magmatism and hydrothermal fluid flow throughout northern Nevada, resulting in structural trends where ore deposits are the largest and most concentrated (Fig. 1) (Hofstra and Cline 2000; Grauch et al. 2003; Cline et al. 2005; Hofstra and Wallace 2006; Cline 2018). Eocene magmatism drove abundant hydrothermal activity throughout the region, mobilizing and redistributing previously concentrated metals. Eocene porphyry Cu-Mo-Au, distal disseminated Au-Ag, and sediment-hosted Carlin-type Au deposits all formed during this time (Hofstra et al. 1999; Ressel and Henry 2006; Muntean et al. 2011). Miocene epithermal Au-Ag mineralization followed (Christiansen et al. 1986; John 2001; Hofstra and Wallace 2006).

Samples and Analytical Methods

Sampling strategy and preparation

Samples in this study represent a suite of igneous rocks from "suspect" magmatic systems contemporaneous with nearby Carlin-type mineralization events in northern Nevada. They are similar in age to mineralization (within analytical error), ranging between ~41–34 Ma. They occur within ~0–5 km of known Carlin-type deposits in the Carlin, Battle Mountain-Eureka, Alligator Ridge, and Long Canyon trends (Fig. 1). For simplicity, we avoided sampling near skarn, epithermal, distal disseminated, or any other deposit types found in the region. Given the focus on "suspect" magmas, rhyolite samples exemplify various eruptive styles and volumes, ranging from meter-wide dikes to caldera-forming ignimbrites. Due to the lack of field relations, none of the samples are considered to be known causative intrusions. An effort was made to include both felsic and mafic samples, but few mafic samples of this age and proximity are exposed (e.g., Ryskamp et al. 2008), and none of the mafic samples we collected (near Eureka, Nevada) had large enough phenocrysts to preserve suitable melt inclusions. Hence, our sample suite includes a range of rhyolite tuffs, porphyritic dikes, a large volume ignimbrite and its post-caldera plutons, and a rhyolite dome. Collectively, our samples represent many volcanic centers that are spatially and/or temporally distinct (Fig. 1; Table 1) and include: (1) tuff samples of Nanny Creek (informally named "Nanny Creek tuffs"), the type location for the Northeast Nevada volcanic field defined by Brooks et al. (1995) in the Long Canyon trend; (2) dike samples from the Beast and Genesis pits (informally named "Beast dike" and "K dike", respectively; Ressel et al. 2000) in the northern Carlin trend; (3) dike samples from the Cortez Hills pit (informally named "Cortez rhyolites" by Henry et al. 2023, further informally broken into "Cortez Hills dikes" including the "Crusher dike," "Middle dike," "F-Canyon dike," and "High Wall dike;" R. Bond, Barrick Gold, personal communication), in the Battle Mountain-Eureka trend; (4) samples of the Caetano Tuff (upper and lower units), Fortress Fault dike (informal name of Colgan et al. 2011), and post-caldera porphyritic intrusions (informally named Carico Lake pluton and Redrock Canyon pluton of John et al. 2008), collectively informally referred to here as the "Caetano caldera suite" in the Battle Mountain-Eureka trend; (5) a dome sample (informally named "Eureka dome") from the Target Hill rhyolite of Hastings (2008) at the southern end of the Battle Mountain-Eureka trend; and (6) a dike sample (informally named "Mooney Basin dike") near Bald Mountain in the informally named "Mooney Basin" of Nutt and Hofstra (2003) at the northern end of the Alligator Ridge trend. A more detailed description of the rhyolite units we sampled and their relationship with nearby mineralization is provided in Online Materials[1] Appendix 1.1.

Carlin-type mineralization is known for its high fluid-to-rock ratios; thus, samples in this study range from relatively fresh (where available) to moderately argillaceous (Table 1). The alteration is biotite and quartz stable, but the feldspars and matrix are highly altered. Therefore, whole rock and matrix glass analyses were unsuitable, and instead, we focused on geochemical analysis of quartz-hosted melt inclusions, quartz, and biotite. Melt inclusions reflect snapshots of the pre-eruptive, volatile-charged magmatic systems. They are complementary to existing whole-rock studies on Eocene magmas in the region, which typically reflect time-integrated late-stage degassed records of magmatism (Esposito et al. 2018). Melt inclusions may also reflect post-entrapment modifications, and we assess this before applying these data for interpretations. Quartz and biotite data provide additional compositional constraints on magmas, and together with melt inclusion compositions, they provide thermobarometric and oxybarometric constraints.

Polished thick sections and grain mounts were prepared for petrographic and scanning electron microscope (SEM) analysis. A portion of each sample was crushed, sieved, and quartz phenocrysts (~0.5–2 mm) hosting suitable silicate melt inclusions (i.e., fully enclosed) were selected and prepared following the basic procedures of Mercer et al. (2015) and recommended best practices of Esposito (2020) and Rose-Koga et al. (2021). About half of the quartz phenocrysts were prepared for direct analysis by LA-ICP-MS, and the other half were reheated to prepare them for analysis by FTIR spectroscopy, EMP, SHRIMP-RG, and LA-ICP-MS.

Quartz phenocrysts with successfully homogenized melt inclusions (i.e., crystals resorbed to glass ± bubble) were mounted individually in acetone-soluble crystal bond on microscope slides and ground and polished to make doubly polished wafers with the melt inclusions exposed on both sides (~15–150 μm thick). After FTIR analyses, wafers were mounted in 1″ epoxy plugs (following the methods used in the Stanford-USGS SHRIMP-RG laboratory) and lightly re-polished for analysis by EMP, SHRIMP-RG, and LA-ICP-MS. Three samples (lower part of Caetano Tuff, 09C3; Carico Lake pluton, 09C7; and Redrock Canyon pluton, 09C10) contained naturally glassy silicate melt inclusions (pure glass) that did not require homogenization, and these were ground and polished for microanalysis following the same methods for homogenized inclusions. Quartz phenocrysts with suitable crystalline silicate melt inclusions were mounted individually in acetone-soluble crystal bond on microscope slides and ground and polished on one side until inclusions were within ~10–80 μm of the polished surface. These grains were then mounted in a 1″ epoxy plug and re-polished so that the melt inclusions could be analyzed for trace elements by LA-ICP-MS. Bulk crystallinity (area%) was estimated quantitatively for a subset of samples (Table 1) using digital images of 6–7 cm wide slabs and the program ImageJ 1.53 (Schneider et al. 2012).

Batch reheating experiments

Batch reheating experiments for a subset of the samples were conducted using zirconium-hafnium-molybdenum (ZHM) cold-seal pressure vessels housed at the U.S. Geological Survey in Menlo Park, California. Quartz crystals were loaded into Pt capsules, which were then crimped and folded to expose grains to the Ar pressure medium and prevent crushing. The capsule was pressurized to the target pressure at room temperature, and then power was applied to heat the capsule to the target temperature over a span of ~30 min. Experiments were run at 140–150 MPa (maintained within ±3 MPa), and the pressure was bled to maintain the target pressure during heating. Experiments were held at the target temperature of 1010 °C (maintained within ±7 °C) for 30–40 min to maximize homogenization and minimize elemental diffusion, following the methods of Mercer et al. (2015). Oxygen fugacity (f_{O_2}) and hydrogen fugacity (f_{H_2}) were not controlled; however, the Mo-bearing pressure vessel buffers the f_{O_2} at reducing conditions of <Mo-MoO_2 (T. Sisson, personal communication), or ~FMQ-4.5 (FMQ = fayalite-magnetite-quartz). Experiments were quenched rapidly (≥200 °C/s) following the method of Sisson and Grove (1993). After quenching, the capsules were opened, and quartz grains hosting glassy, fully enclosed silicate melt inclusions were selected for analysis. Additional experimental details are reported in Online Materials[1] Appendix 1.2.

Analytical methods

Fourier transform infrared (FTIR) spectroscopy. Water and CO_2 concentrations dissolved in 110 glassy (reheated) silicate melt inclusions were measured using a Bruker Vertex 70 FTIR spectrometer interfaced with a Hyperion 3000

Table 1. Sample overview

Trend	Location	Sample name	Sample no.	Unit	Latitude	Longitude	Rock type	Crystallinity (avg. area%)	Mineralogy (±alteration)	Alteration	Igneous age (Ma ± 2σ)	Carlin-type Au deposit nearby	Carlin-type Au deposit age (Ma)	Interpreted timing[a]	Reference
Long Canyon	Nanny Creek	Nanny Creek tuff	13NC1	T3a	41.0251	−114.5293	Rhyolite tuff	NA	ab, san, qz, bi, mag, ilm, ap, zr	Fresh	39.61(±0.26)	Long Canyon	39–41	Syn-ore	12, 13, 14, 15
		Nanny Creek tuff	13NC3	T1	41.0238	−114.5472	Rhyolite tuff	NA	ab, san, qz, bi, mag, ilm, ap, zr	Fresh	41.08(±0.22)	Long Canyon	39–41	Syn-ore	12, 13, 14, 15
Carlin	Beast pit	Beast dike	13BST4	Ei	40.9417	−116.3550	Porphyritic dike	27	ab, san, qz, bi, mag, ap, zr	Moderate argillic	37.55(±0.14)	Beast	<37.3	Pre-ore	1, 2
	Genesis pit	K dike	13K1	Ei	40.9446	−116.3699	Porphyritic dike	NA	ab, san, qz, bi, mag, ap, zr	Mild argillic	40.3(±0.4)	Genesis	<40.3	Pre-/syn-ore	1, 3
Battle Mountain-Eureka	Caetano caldera suite	Lower Caetano Tuff	13CC3	Tcl	40.1564	−116.6474	Intra-caldera tuff	38	ab, san, qz, bi, Fe-Ti, ap, zr, opx	Fresh	34.0(±0.1)	Cortez Hills	35.71(±0.07)	Post-ore	4, 5, 6, 7
		Lower Caetano Tuff	13CC6	Tcl	40.1864	−116.8047	Intra-caldera tuff	38	ab, san, qz, bi, Fe-Ti, ap, zr, opx	Fresh	34.0(±0.1)	Cortez Hills	35.71(±0.07)	Post-ore	4, 5, 6, 7
		Lower Caetano Tuff	09C3	Tcl	40.0819	−116.6820	Intra-caldera tuff	38	ab, san, qz, bi, Fe-Ti, ap, zr, opx	Fresh	34.0(±0.1)	Cortez Hills	35.71(±0.07)	Post-ore	4, 5, 6, 7
		Upper Caetano Tuff	13CC5	Tcu	40.1889	−116.7901	Intra-caldera tuff	40	ab, san, qz, bi, Fe-Ti, ap, zr, opx	Fresh	33.91(±0.04)	Cortez Hills	35.71(±0.07)	Post-ore	4, 5, 6
		Upper Caetano Tuff	13CC7	Tcu	40.1887	−116.7929	Intra-caldera tuff	40	ab, san, qz, bi, Fe-Ti, ap, zr, opx	Fresh	33.91(±0.04)	Cortez Hills	35.71(±0.07)	Post-ore	4, 5, 6
		Fortress Fault dike	13CC4	Tcf	40.1771	−116.6568	Porphyritic dike	NA	ab, san, qz, bi, Fe-Ti, ap, zr	Moderate argillic	34.00(±0.05)	Cortez Hills	35.71(±0.07)	Post-ore	4, 5, 6
		Carico Lake pluton	09C7	Tcc	40.1672	−116.8486	Post-caldera pluton	61	ab, san, qz, bi, Fe-Ti, ap, zr, hbl	Mild argillic	34.00(±0.05)	Cortez Hills	35.71(±0.07)	Post-ore	4, 5, 6
		Redrock Canyon pluton	09C10	Tcr	40.1413	−116.9021	Post-caldera pluton	40	ab, san, qz, bi, Fe-Ti, ap, zr, hbl	Mild argillic	33.90(±0.05)	Cortez Hills	35.71(±0.07)	Post-ore	4, 5, 6
	Cortez Hills pit	Crusher dike	13CH3a	Tpr	40.1680	−116.6059	Porphyritic dike	11	ab, san, qz, bi, ap, zr	Mild argillic	35.70(±0.05)	Cortez Hills	35.71(±0.07)	Syn-/post-ore	4
		Crusher dike	13CH3b	Tpr	40.1680	−116.6059	Porphyritic dike	NA	ab, san, qz, bi, ap, zr	Mild argillic	35.70(±0.05)	Cortez Hills	35.71(±0.07)	Syn-/post-ore	4
		Middle dike	13CH6	Tpr	40.1712	−116.6084	Porphyritic dike	NA	ab, san, qz, bi	Mild argillic	35.70(±0.05)	Cortez Hills	35.71(±0.07)	Syn-/post-ore	4
		F-Canyon dike	13CH7	Tpr	40.1712	−116.6087	Porphyritic dike	20	ab, san, qz, bi	Moderate argillic	35.70(±0.05)	Cortez Hills	35.71(±0.07)	Syn-/post-ore	4
		High Wall dike	13CH10	Tpr	40.1662	−116.5979	Porphyritic dike	17	ab, san, qz, bi, ap, zr	Mild argillic	35.70(±0.05)	Cortez Hills	35.71(±0.07)	Syn-/post-ore	4
	Target Hill	Eureka dome	13E1	Trt	39.5079	−115.9760	Rhyolite dome	20	ab, san, qz, bi, ilm, ap, zr	Fresh	35.4(±0.2)	Archi-medes/ Ruby Hill	>36	Post-ore	8, 9
Alligator Ridge	Bald Mountain	Mooney Basin dike	13BM1	Tvi	39.9012	−115.4579	Porphyritic dike	14	ab, san, qz, bi, ap, zr	Fresh	35.9(±0.1)	Galaxy, Horseshoe, Saga	<45, >34	Syn-/post-ore	8, 10, 11

Notes: NA = not analyzed; ab = albite; san = sanidine; qz = quartz; bi = biotite; Fe-Ti = Fe-Ti oxide; mag = magnetite; ilm = ilmenite; ap = apatite; zr = zircon; opx = orthopyroxene; hbl = hornblende. References: (1) Ressel and Henry 2006; (2) Ressel et al. 2000; (3) Farmer 1996; (4) Henry et al. 2023; (5) John et al. 2008; (6) Colgan et al. 2011 (7) Watts et al. 2016; (8) Mortensen et al. 2000; (9) Dilles et al. 1996; (10) Nutt 2000; (11) Nutt and Hofstra 2003; (12) Brooks et al. 1995; (13) Smith et al. 2013; (14) Chakurian et al. 2003; (15) Tretbar et al. 2000.

[a] Based on geologic and geochronologic evidence.

FTIR microscope housed at the U.S. Geological Survey Denver Inclusion Analysis Laboratory. The FTIR spectrometer and microscope stage were continuously purged with dry, CO_2-free air to avoid interference by atmospheric H_2O and CO_2. Measured relative absorbances were converted to H_2O and CO_2 concentrations using the Beer-Lambert Law, $c_i = M_iA/\rho d\varepsilon$, where c_i is the concentration of the absorbing species, M_i is the molecular weight of the H_2O (18.02) or CO_2 (44.00), A is the absorbance intensity of the band of interest, ρ is the room temperature density of the rhyolitic glass, d is the thickness of the inclusion [measuring thickness following methods of Mercer (2021)], and ε is the molar absorption coefficient for the species of interest. Based on replicate FTIR analyses, 2σ precision is generally within ≤0.1 wt% for H_2O and ≤15 ppm for CO_2. Online Materials[1] Appendix 1.3 contains data reduction details.

Scanning electron microscope (SEM) and electron microprobe (EMP) analyses. SEM and EMP data were obtained at the U.S. Geological Survey Denver Microbeam Laboratory. Sample imaging and laser/ion beam pit observations were acquired using the FEI Quanta 450 field emission gun SEM at the Denver Microbeam Laboratory operating at 15kV and a beam current of 0.1–0.5 nA. Major and minor elements in 129 glassy melt inclusions (naturally glassy and homogenized) were analyzed by EMP using a JEOL 8900 electron microprobe at the U.S. Geological Survey Denver Microbeam Laboratory. Analyses employed a setup optimized for hydrous glass using a 15 kV accelerating voltage, 10 nA beam current, and the largest spot size possible (~3–10 μm) to minimize volatilization (e.g., Morgan and London 1996). Na, K, Si, and Al were counted first to collect X-rays with minimal beam exposure. Their concentrations were then calculated using a time-dependent intensity correction in Probe for Windows (Donovan et al. 2011) to minimize the effects of alkali migration. Analyses of Cl and F in the glass inclusions were well above the detection limit (90 and 1240 ppm, respectively), whereas nearly all analyses of S were below the detection limit (130 ppm), so we used SHRIMP-RG to measure S contents. Biotite was analyzed using a 15 kV accelerating potential, a 20 nA beam current, and a 1–5 μm spot size. Natural and synthetic minerals and glasses were used as standards for all EMP analyses. For oxide concentrations >1 wt%, 1σ uncertainties are generally <3% relative, while for oxide concentrations <1 wt%, 1σ uncertainties are generally <10% relative. A summary of the average detection limits and reproducibility of our in-house rhyolite and biotite reference materials are reported in Online Materials[1] Appendix 1.4.

Laser ablation-inductively coupled plasma-mass spectrometry (LA-ICP-MS). Trace elements were analyzed from 154 silicate melt inclusions (33 naturally glassy, 57 reheated glassy, 64 crystalline) by LA-ICP-MS at the University of Toronto using a NWR 193 nm UC laser ablation system and an Agilent 7900 quadrupole mass spectrometer. Major elements were analyzed to help monitor for analysis contamination and to compare Na values among unheated and reheated inclusions. One laser ablation setup was optimized for spot analyses of homogeneous glass inclusions, and another for drilling through quartz and analyzing whole crystalline inclusions. The NIST 610 glass was used as the primary reference material for all analyses, and GSD-1G was used as the secondary standard for all analyses. The preferred standard values for these standard glasses are from Jochum et al. (2011) and GeoRem (http://georem.mpch-mainz.gwdg.de). Relative precision for analyses is <10% based on replicate analyses of the GSD-1G glass. A summary of the analytical conditions, data acquisition parameters, reproducibility of the GSD-1G glass, and average detection limits for each element are reported in Online Materials[1] Appendix 1.5.

Sensitive high-resolution ion microprobe-reverse geometry (SHRIMP-RG) analyses. A suite of five trace elements that are difficult to resolve by EMP or LA-ICP-MS (Li, B, P, S, Se) was analyzed in 87 glassy melt inclusions (naturally glassy and homogenized) by ion microprobe at Stanford University using the Australian Scientific Instruments Stanford/USGS SHRIMP-RG. Glassy silicate melt inclusions were analyzed by operating the SHRIMP-RG with a 5 nA Cs^+ primary beam focused to a 20 μm spot size. Elemental concentrations were calculated by calibrating a York linear regression to the average standard data for the ATHO-G, NIST 611, NIST 613, and NIST 615 standard glasses. Relative precision is <10% for Li, P, and S, and <20% for B and Se based on replicate analyses of glass standards. A summary of the analytical conditions, data acquisition parameters, elemental calibrations, and average detection limits are reported in Online Materials[1] Appendix 1.6.

Results

Sample petrography

Porphyritic hand specimens range from relatively fresh to mild- or moderate-argillaceous alteration (Table 1; Online Materials[1] Appendix 1.7). Samples with argillic alteration preserve rounded quartz phenocrysts (~0.5–4 mm), partly- to completely altered white to orange plagioclase and alkali feldspar laths (0.5 mm to 2 cm), and where argillic alteration is only weak, black biotite books are preserved that contain inclusions of apatite, zircon, ±sanidine, ±plagioclase (oligoclase, andesine, laboradorite), ±ilmenite, ±magnetite (note: unlike porphyry Cu-style alteration, Carlin-style alteration is typically biotite stable). Topaz has been identified in the lower part of the Caetano Tuff (Watts et al. 2016). Samples range from ~10–60 vol% phenocrysts (Table 1). Clear to smoky quartz phenocrysts are unaltered and host abundant silicate melt inclusions. Reheated quartz phenocrysts are typically clear. Biotite phenocrysts are typically sparse (<1–3 vol%) and occur as thin books ~0.1–3 mm in length. The books are euhedral to subhedral, and samples are typically cohesive and unaltered with mineral inclusions including zircon, fluorapatite, andesine-labradorite, sanidine, ilmenite, and Ti-magnetite.

Silicate melt inclusions are composed of variably devitrified glass, ±quartz, ±sanidine, ±FeTi oxides, and ±bubbles. About 15% of inclusions were naturally glassy (in three samples) but the rest were partly to wholly crystalline. Inclusions vary in size (~10–160 μm) and are generally equant with rounded or negative bipyramidal forms. After laboratory homogenization, inclusions are composed of clear glass, and about one-third contain bubbles (more details about bubble-bearing inclusions, below).

Melt inclusion post-entrapment modification summary

This study encompasses results from microanalysis of 234 melt inclusions, including 33 naturally glassy, 137 reheated glassy, and 64 unheated crystalline inclusions. Post-entrapment crystallization and diffusion are known to modify original melt inclusion compositions (e.g., Kamenetsky and Danyushevsky 2005; Zajacz et al. 2009; Rottier et al. 2017; Ellis et al. 2018; Neukampf et al. 2019; Rose-Koga et al. 2021; Esposito et al. 2023). A detailed assessment of post-entrapment modifications for these samples is provided in Online Materials[1] Appendix 1.8; a summary is provided here. A comparison of compositions of reheated (glassy) and unheated (crystalline and naturally glassy) melt inclusions from each magmatic center shows that reheated inclusions are effectively indistinguishable from unheated inclusions to within 1σ standard deviation for all elements except univalent cations (Online Materials[1] Appendix Fig. A1.8.1). Therefore, we do not distinguish between them with symbology moving forward in the manuscript.

Univalent cations, including Na^+, H^+, and Li^+, may be prone to notable post-entrapment diffusion (e.g., Severs et al. 2007; Zajacz et al. 2009). Diffusion can be challenging to quantify because it overprints the natural variability within samples and can occur during natural post-entrapment processes (e.g., cooling of a tuff or dike) and/or during reheating experiments. Therefore, we assessed these elements more carefully. A comparison of Na_2O contents measured in reheated and unheated inclusions for each sample shows that measured Na_2O contents from most samples are indistinguishable to within 1σ standard deviation. All samples are indistinguishable to within 2σ standard deviations (Online Materials[1] Appendix Fig. A1.8.2.). Based on this observation, we conclude that Na^+ migration during EMP analyses was

effectively minimized using the time-dependent intensity correction in Probe for Windows (Donovan et al. 2011) and that the majority of post-entrapment migration of Na^+ that may have taken place likely occurred by natural diffusion (i.e., in the ground) rather than during reheating experiments. Thus, we present data for Na_2O from both unheated and reheated inclusions, but consider that lower Na_2O contents (~2 wt% normalized volatile-free) may be minimum estimates due largely to natural diffusion. Low Na_2O contents do not correlate with unusually high ASI values (Online Materials[1] Appendix Fig. A1.8.3). In general, high ASI values may be found over the entire range of Na_2O contents regardless of whether inclusions were reheated or not.

Given the relatively smaller ionic radius and faster diffusion rates of H^+ and Li^+ compared to Na^+, we assume that these elements probably diffused out of melt inclusions to some extent both naturally and experimentally (e.g., Zajacz et al. 2009; Ellis et al. 2018; Neukampf et al. 2019). A comparison of Li contents from reheated and unheated inclusions (with all samples treated together) indicates Li-loss from reheated inclusions, perhaps by ~75% on average (Online Materials[1] Appendix Fig. A1.8.4). However, Li-loss does not appear to have been catastrophic, i.e., some reheated inclusions still contain up to several 100 ppm Li, which is a significant amount for rhyolite melt. We therefore believe these data are valuable to identify Li-bearing systems and place constraints on minimum Li values. Because post-entrapment diffusive hydrogen-loss (H_2, H_2O, and/or H^+) is likely, but we only have H data for reheated inclusions, we calculated restored H_2O contents based on H_2O/Nb partitioning following the preferred method of Myers et al. (2016, 2019) before applying these data for interpretative purposes (details in Online Materials[1] Appendix 1.8.3). Based on this restoration method, we estimate that the average amount of overall diffusive hydrogen loss was ~35%. Note that not all melt inclusions with measured H_2O have Nb measurements that can be used for restoration, and therefore we report both measured H_2O and restored H_2O values (Online Materials[1] Appendix 2).

The majority of melt inclusions in this study are bubble-free; however, about one-third of inclusions contain bubbles that represent either co-trapped supercritical fluid or post-entrapment leakage that could signal fluid/melt partitioning of CO_2 and/or loss of mobile elements (e.g., Lowenstern 2015; Moore et al. 2015). About half of the bubble-bearing inclusions contain <10 vol% bubbles and show minimal loss of CO_2, whereas the other half contain ≥10 vol% bubbles with extensive CO_2-loss (Online Materials[1] Appendix 1.8.4). In bubble-bearing melt inclusions, CO_2 values should be considered minimum estimates. There is no correlation between bubble vol% and Na_2O, H_2O, or Li contents; therefore, we do not consider leakage to be a major problem in bubble-bearing samples.

Samples in this study range from rhyolite to high-silica rhyolite, with some notably high SiO_2 contents when considered on a volatile-free basis (~71.5 to 84.5 wt% SiO_2). We do not observe any correlations between melt inclusion size and SiO_2 (or Na_2O, Li, or H_2O). A thorough assessment of this observation is provided in Online Materials[1] Appendix 1.8.5. Given that we find no evidence for analytical errors or probable post-entrapment modification problems that would lead us to eliminate these data, and that there is a precedent for such high SiO_2 values in the literature (e.g., Norling et al. 2016; Zhang and Audétat 2017; Fiedrich et al. 2020; Rottier et al. 2020; Butters et al. 2025), we conclude that the SiO_2 values reported in this study are reasonable for hydrous silicate melts and treat them as such moving forward.

Melt inclusion compositions

In addition to this publication (Online Materials[1] Appendix 2), raw geochemical data are published and available in Mercer and Hofstra (2020). Silicate melt inclusions are rhyolite to high-silica rhyolite (77.2 ± 3.6 wt% SiO_2, normalized volatile-free) with Na_2O+K_2O ranging broadly from ~4.7 to 10.8 wt%, overlapping with the most evolved Eocene igneous whole rock samples from the region (Online Materials[1] Appendix 3.1). Melts represent evolved compositions spanning from calc-alkaline to shoshonite series of Le Maitre (1989), calcic to alkalic series of Frost and Frost (2008), and are ferroan [Fe/(Fe+Mg) > 0.8; Frost and Frost (2011); Fig. 2a; Online Materials[1] Appendix 3.1]. A few melts are metaluminous, but most range from weakly peraluminous to strongly peraluminous (aluminum saturation index, ASI > 1.1), while some are remarkably hyperaluminous (ASI > 1.3). These compositions overlap with other evolved Eocene igneous whole rock data throughout northern Nevada (Fig. 2b), whose peraluminous to strongly peraluminous character has been attributed to abundant pelitic or quartzofeldspathic crustal sedimentary sources in the region (du Bray 2007). The strongly peraluminous character of the melts is mirrored by high ASI values of coexisting biotite (see biotite results below). While there is a conspicuous lack of peraluminous phenocrysts observed in hand samples (e.g., topaz, muscovite, leucite, garnet, cordierite), which we might expect to observe in peraluminous magmas (e.g., Christiansen et al. 1983; Webster et al. 1987; Acosta-Vigil et al. 2003), their absence is sensible considering that melt entrapment pressures, temperatures, and crystallinities appear to be outside of the stability fields of these minerals (see thermobarometry and phase equilibria results below for more explanation on the stability of these phases). In other words, when these melts were trapped, they had not yet saturated with a peraluminous mineral phase aside from biotite.

Rhyolite and high-silica rhyolite melts display wide variations in trace element concentrations. Chondrite-normalized rare earth element (REE) concentrations span one to two orders of magnitude among the various volcanic centers. Rare earth element patterns typically have gentle to steep negative slopes (Fig. 2c; La/Yb_{CN} ~2–30, Online Materials[1] Appendix 3.2), with light rare earth elements (LREEs) generally enriched relative to heavy rare earth elements (HREEs). Europium anomalies range from extremely negative to nonexistent (Eu/Eu* ~0.02–1.0, Online Materials[1] Appendix 3.2). Samples with higher overall REE concentrations (e.g., Caetano caldera suite, Eureka dome) tend to have flatter patterns (La/Yb_{CN} ~1–10) with more pronounced negative Eu anomalies (Eu/Eu* ~0.02–0.5) than samples with lower overall REE concentrations (e.g., Beast dike). A chondrite-normalized multi-element spider diagram generally shows a broad range of trace element behavior, with moderate to deep troughs in Ba, Sr, P, and Ti in some samples, indicative of crystallization of sanidine, plagioclase, apatite, monazite, and Fe-Ti oxides, and notable enrichments in Rb, Ba, Th, U, Nb, Ta, La,

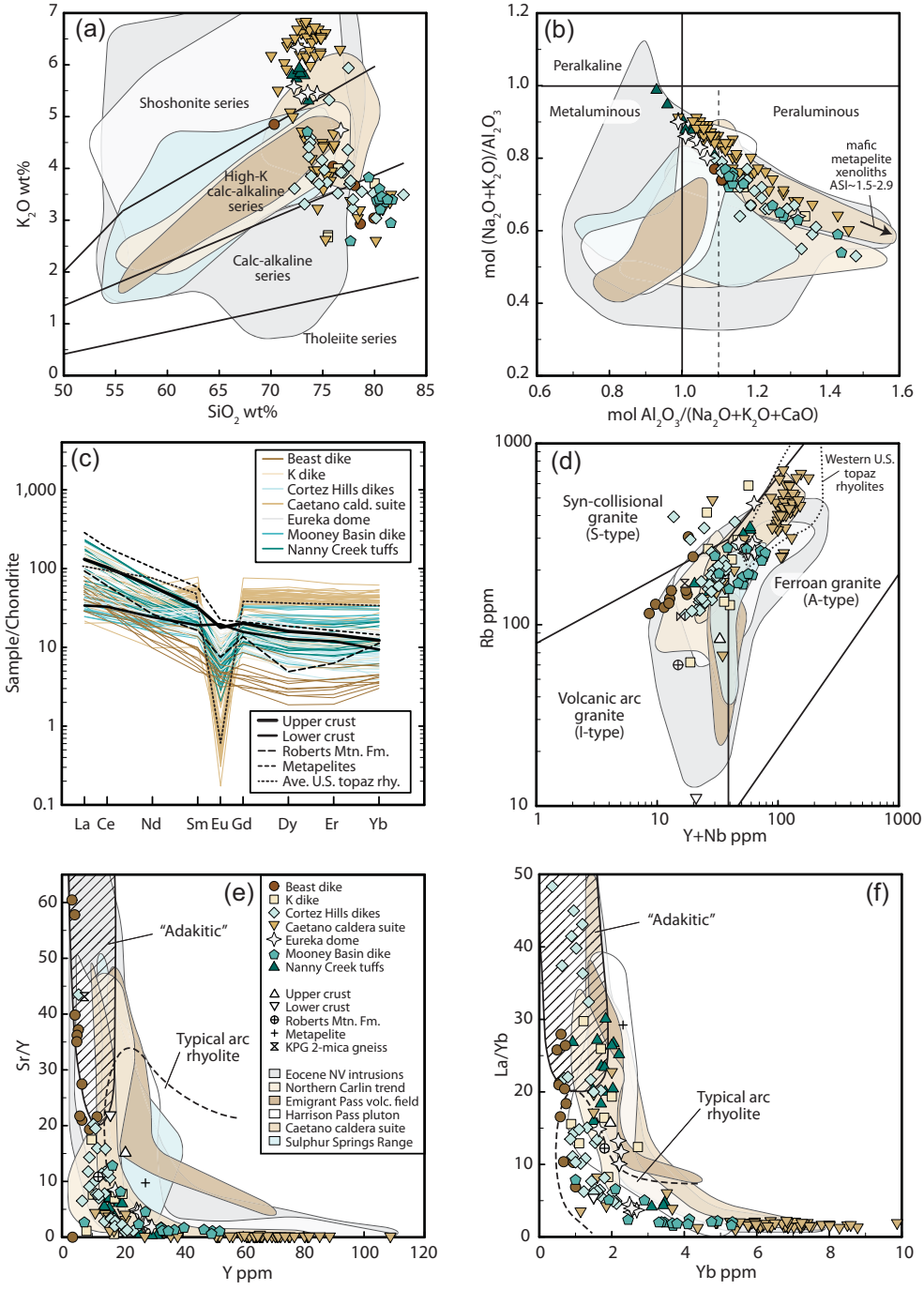

Figure 2. (**a**) Classification of igneous rocks based on potassium (Le Maitre 1989). (**b**) Aluminum saturation index and alkalinity index (Frost and Frost 2008). The arrow indicates the trajectory to mafic metapelite xenoliths hosted in the Carico Lake pluton, which represent a hyperaluminous crustal component in the region, similar to the Neoproterozoic miogeoclinal metasediments of the McCoy Creek Group (Watts et al. 2016). (**c**) Chondrite normalized rare earth element patterns (CI chondrite) (McDonough and Sun 1995). (**d**) Granitoid discrimination diagram (Pearce et al. 1984; Frost and Frost 2011). Dashed field represents whole-rock data from western U.S. topaz rhyolites (Ave. U.S. topaz rhy.) (Christiansen et al. 1986). (**e**, **f**) "Adakitic" signatures and typical arc rhyolite signatures [fields from Richards and Kerrich (2007); Castillo (2012)]. Estimated 1σ uncertainties are smaller than symbols. Regional igneous whole rock data are shown for comparison [Eocene Nevada intrusions (du Bray 2007); northern Carlin trend igneous suite (Ressel and Henry 2006); Emigrant Pass volcanics (Johnson et al. 2015); Harrison Pass pluton (Barnes et al. 2001); Caetano caldera suite (Watts et al. 2016); volcanics of the Sulfur Springs Range (Ryskamp et al. 2008)]. Also for comparison are average upper crust (i.e., representing shales, sediments, and intrusions) and lower crust (mafic-felsic amphibolite and granulite, anorthosite, and eclogite) from Rudnick and Gao (2014); black calcareous mudstone of the Paleozoic Roberts Mountains Formation (Roberts Mtn. Fm.) (Large et al. 2011); Neoproterozoic miogeoclinal metapelites of the McCoy Creek Group (Lee et al. 2003), and a Mesozoic two-mica granitic gneisses (KPG = pegmatitic two-mica granitic gneiss formed by muscovite dehydration) (Lee et al. 2003).

and Y relative to average upper crust in other samples (Online Materials[1] Appendix 3.2).

Melt trace element compositions plot across volcanic arc (I-type) granite to within-plate (A-type) granite (more specifically, "ferroan" rhyolite; Frost and Frost 2011) fields of the tectonic discrimination diagrams of Pearce et al. (1984), with a few plotting in the syn-collisional (S-type) granite fields (Fig. 2d). Note that throughout this paper for simplicity we use "I-type" and "A-type" primarily to describe an assortment of geochemical characteristics (Bonin 2007; Frost and Frost 2011; Chappell et al. 2012), not to imply specific tectonic interpretations. This compositional spectrum was initially surprising, given the relatively short ~7 m.y. timespan of the sample suite, but intriguing given the geodynamics of the region, and we discuss our preferred tectonic-magmatic interpretation later. Melts also encompass a large range of Sr/Y and La/Yb, with many samples characteristic of typical arc rhyolites, whereas others trend toward "adakitic" signatures (Figs. 2e and 2f) (Richards and Kerrich 2007; Castillo 2012). Here we use the term "adakitic" in a compositionally descriptive sense, referring to a sub-type of calc-alkaline rocks formed from melts that are chemically distinguishable from ordinary calc-alkaline silicate rocks by high $Al_2O_3 > 15$ wt%, high $Sr/Y > 20$, high $La/Yb > 20$, low $Y < 18$ ppm, and low $Yb < 2$ ppm (e.g., Richards and Kerrich 2007; Loucks 2021). We discuss our preferred petrogenetic interpretation of "adakitic" signatures later.

Melts contain a wide range of dissolved volatile concentrations (Online Materials[1] Appendices 2 and 3.3). Measured dissolved H_2O contents range from ~0.3 to 4.7 wt% (median ~2.6 wt%) and restored H_2O contents range from ~0.6 to 5.2 wt% (median ~4.3 wt%). Dissolved CO_2 concentrations range from ~20 to 950 ppm (median ~116 ppm; values <100 ppm considered minimum estimates). Dissolved CO_2 and restored H_2O contents in melts from each magma center define relatively ideal decompression degassing paths (i.e., defined by steep drops in CO_2 starting from less than ~300 MPa with small changes in H_2O) for H_2O-rich samples with some likely contributions from isobaric fluid-saturated crystallization and/or CO_2 flushing (Newman and Lowenstern 2002; Caricchi et al. 2018), whereas H_2O-poor samples are likely fluid-undersaturated (Fig. 3a). Fluorine and Cl concentrations are moderate to very high, from ~1280 (~3 times higher than F contents in average continental rhyolite; Robb 2020) to 10 700 ppm F (median ~1710 ppm F) and ~110 to 1900 ppm Cl (median ~570 ppm Cl), respectively. Rhyolite melts from the Caetano caldera suite and Mooney Basin dike have notably higher F contents, whereas those from the Nanny Creek tuffs have markedly higher Cl contents than the other volcanic centers. Sulfur contents are low, ~2 to 140 ppm (median ~13 ppm), as expected due to the low solubility of sulfur in rhyolite melts (Wallace and Edmonds 2011). Lithium concentrations are low to quite high, from ~1 to 490 ppm (median ~88 ppm). Cl/H_2O ratios are distinct between H_2O-rich and -poor samples (Online Materials[1] Appendix 3.4).

Melt Inclusion Entrapment Thermobarometry

Melt inclusion entrapment temperatures were calculated using our preferred zircon saturation thermometer of Watson and Harrison (1983; see Online Materials[1] Appendix 1.9 for details about the preferred method), yielding temperatures from 673 to 778 °C (median 720 °C). This is in relative agreement with mean magnetite-ilmenite equilibrium temperatures ~745 °C reported from the Caetano Tuff (Watts et al. 2016). Melt inclusion entrapment pressure estimates were calculated by our preferred method (Mercer 2021) using the Ti-in-quartz thermobarometer of Huang and Audétat (2012) in conjunction with the rutile solubility model of Kularatne and Audétat (2014), assuming the temperatures above. Concentrations of Ti in host quartz were measured by LA-ICP-MS during drilling to crystalline inclusions and correspond to quartz spatially adjacent to the analyzed inclusion. Concentrations range from 6 to 95 ppm Ti (median 37 ppm; Online Materials[1] Appendix 2). To produce pressure estimates for exposed glassy inclusions (i.e., for which we do not have direct quartz analyses), the average Ti concentration in quartz from each sample was used. The calculated activity of TiO_2 (a_{TiO_2}) ranges from 0.02 to 0.83 (median 0.17). This technique yields pressures ranging from 1 to 906 MPa, with most inclusions returning pressures ≤300 MPa (median 168 MPa). These pressures correspond to depths of ~0.03 to 24 km (median 4.7 km) assuming a metasediment crustal density of ~2.67 g/cm^3 (Grauch et al. 2003). Thermobarometry results are summarized in P-H_2O and P-T diagrams (Figs. 3b and 3c). Estimated 1σ uncertainties are ±15 °C and ±12 MPa (Boehnke et al. 2013; Zhang et al. 2020).

We also calculated vapor saturation pressures for each inclusion using the MagmaSat H_2O-CO_2 fluid saturation model of Ghiorso and Gualda (2015) and the measured dissolved CO_2 and restored H_2O contents. This method yields pressures from 18 to 266 MPa (median 170 MPa; Online Materials[1] Appendix 2), corresponding to depths of ~0.5 to 7.1 km (median 4.8 km). These pressure estimates can vary considerably from those using the technique above; however, average pressures returned are very similar (e.g., Mercer 2021). Due to possible errors introduced by CO_2- and H_2O-loss, we prefer the Ti-in-quartz/rutile solubility technique and present only the results from this method for interpretive purposes throughout the rest of the paper.

Phase equilibria thermodynamic model

Also shown on the pressure-temperature diagram (Fig. 3c) are modeled equilibrium phase relations for the average melt inclusion composition (Online Materials[1] Appendix 2) generated using Rhyolite-MELTS v.1.1.0 (Gualda et al. 2012). Models were run with an oxygen fugacity of ΔNNO (i.e., at the nickel-nickel-oxide buffer) based on redox estimates from coexisting biotite (detailed below). Phase equilibria reproduce the main sample mineralogy (e.g., quartz, plagioclase, sanidine, biotite, Fe-Ti-oxides), but do not include all minor or accessory phases (e.g., pyroxenes, hornblende, zircon, allanite) as expected given the model's limitations for these minerals (P. Asimow, personal communication). Notably, modeling results support the presence of peraluminous minerals garnet, muscovite, and leucite, which we expect to observe in these peraluminous magmas, but only at significantly higher pressures and/or lower temperatures than the conditions of melt inclusion entrapment. At lower pressures and temperatures, topaz is observed as a stable peraluminous accessory phase in experiments of hydrous, F-bearing (A-type) granitic melts (Webster et al. 1987), while cordierite is observed as a stable peraluminous phase in equilibrium experiments of hydrous,

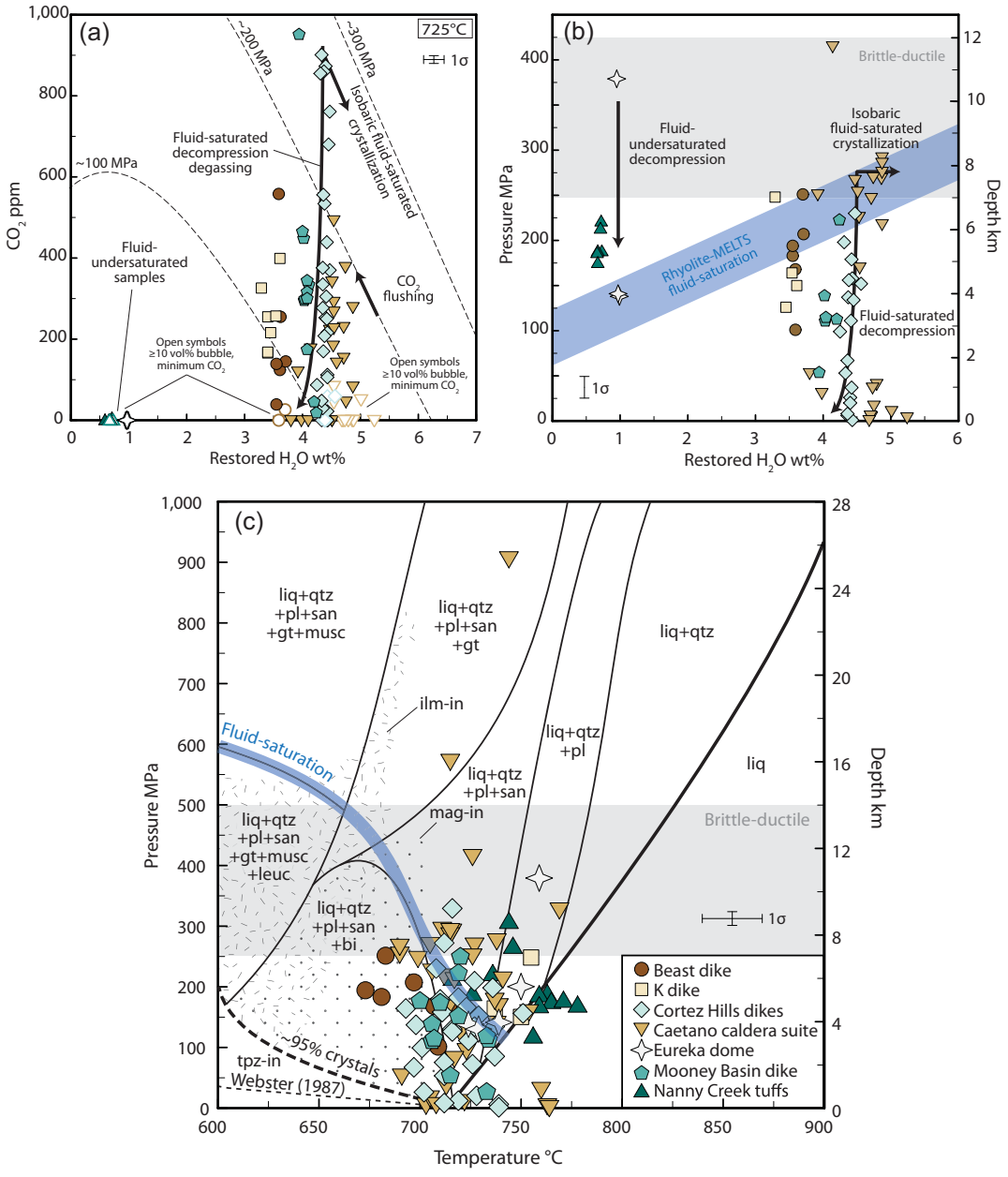

Figure 3. Fluid saturation conditions and phase equilibria of melts. (**a**) Melt inclusion CO_2 and restored H_2O concentrations. Open symbols represent inclusions with ≥10 vol% bubbles and represent minimum estimates for CO_2 (Online Materials[1] Appendix 1.8.4). For general reference, fluid-saturation isobars (725 °C) from Liu et al. (2005) are shown for simple H_2O-CO_2 systems (e.g., F- and Cl-free), assuming fluid saturation. Note that these isobars are for general reference and are not our preferred barometry method (see text for details). Example open and closed-system degassing paths from Newman and Lowenstern (2002) and isobaric CO_2 flushing paths from Caricchi et al. (2018) are shown for general reference. Estimated error bars (left) show average 1σ standard deviation for multiple analyses. (**b**) Quartz-hosted melt inclusion barometry results, using our preferred barometry method (see text for details), shown as a function of restored H_2O contents. Fluid-saturation pressures from Rhyolite-MELTS modeling are also shown with a blue band and indicate that most of the H_2O-rich samples were fluid-saturated upon decompression. (**c**) Thermobarometry summary for melt inclusion entrapment conditions (using preferred thermobarometry methods, details in text). Modeled phase equilibria using Rhyolite-MELTS (Gualda et al. 2012) are shown for the average melt inclusion composition in this study (Online Materials[1] Appendix 2) (Mercer and Hofstra 2020). Note, these phase relations should be used as a general guide since variations in F and H_2O contents among volcanic centers can change the specific phase equilibria and fluid-saturation boundaries. Phases include: silicate liquid (liq), quartz (qtz), plagioclase (pl; andesine-oligoclase), sanidine (san), ilmenite (ilm), magnetite (mag), biotite (bi), garnet (gt), muscovite (musc), leucite (leuc), and topaz (tpz). Estimated 1σ uncertainties are shown in each figure.

peraluminous (S-type) granitic melts (Acosta-Vigil et al. 2003). Topaz is not expected to saturate until very near the solidus (~5% melt remaining, within ~50 °C of the solidus) (Webster et al. 1987), however, and is often not observed as phenocrysts in "topaz" rhyolite rocks, but rather as a fine-grained groundmass phase or in vapor phase mineralization (Christiansen et al. 1983). Since Rhyolite-MELTS cannot handle near- or sub-solidus phase equilibria, we estimate the fluid-saturated solidus based on the highest crystal fraction calculations (~95% crystals) and F-bearing rhyolite experiments of Webster et al. (1987) (1.2 wt% F).

Biotite compositions, thermometry, and oxygen barometry

We analyzed biotite from 12 samples, representing all volcanic centers in this study (Online Materials[1] Appendix 2). Biotite compositions reflect relatively high alumina activity, with most ASI values >1.4 (median 1.43), consistent with peraluminous coexisting melt compositions (Zen 1988). Halogen ratio intercept values [i.e., an indicator of halogen activity in the magmatic system, corrected for the Mg/Fe ratio in biotite; Munoz 1984; $IV(F) = 1.52\,X_{phlogopite} + 0.42\,X_{annite} + 0.20\,X_{siderite} - \log(X_F/X_{OH})$; $IV(Cl) = -5.01 - 1.93\,X_{phlogopite} - \log(X_{Cl}/X_{OH})$; $IV(F/Cl) = IV(F) - IV(Cl)$] are diverse, ranging from ~6.0 to 4.0 IV(F/Cl) indicating a broad range of halogen enrichment among the magmatic centers (Fig. 4a; Online Materials[1] Appendix 3.5). Biotite compositions from samples with more I-type affinity tend to overlap with those from biotite granites (i.e., less peraluminous granites) and Au-, Cu-, and Sn-W-Be-mineralized systems, whereas those from samples with more A-type affinity tend to overlap more with two-mica (i.e., more highly peraluminous granites) and Sn-W-Be mineralized systems (Fig. 4a; Online Materials[1] Appendix 3.5) (Munoz 1984; Zhang et al. 2016; Jin et al. 2018).

Biotite precipitation temperature estimates were calculated using the empirical X_{Mg}-Ti-in-biotite thermometer of Henry et al. (2005) (Online Materials[1] Appendix 2). Results for these samples yield temperatures of ~640 to 770 °C (median 728 °C; Fig. 4b), overlapping with many melt inclusion entrapment temperatures above (Fig. 3).

Due to the lack of coexisting Fe-Ti oxides observed in the samples, we used the biotite composition as a proxy for f_{O_2} (e.g., Shabani et al. 2003). The molar ratio of Fe/(Fe+Mg) in biotite ranges from ~0.35 to 0.95 (median 0.64; Fig. 4b). Most samples contain Fe-dominant compositions [>0.5 Fe/(Fe+Mg)], consistent with the ferroan character of coexisting melts for those samples. Iron-rich biotite suggests equilibration at moderately oxidized to oxidized conditions (~ΔNNO-1.0 to ΔNNO+2.0), with the most Fe-rich biotite from the Caetano Tuff suggesting equilibration at more reduced conditions (~ΔNNO-0.5). This is consistent with estimates of ~ΔNNO-1.07 from Fe-Ti oxide oxybarometry of the Caetano Tuff (Watts et al. 2016). Dike samples from the Carlin trend (Beast and K dikes) contain Mg-dominant biotite [<0.5 Fe/(Fe+Mg)], which is consistent with coexisting melts from these samples that are slightly less ferroan (Online Materials[1] Appendix 3.1). The Mg-dominant biotite hosted in the Beast and K dikes from the Carlin trend suggests equilibration at more oxidized conditions (>ΔNNO+2.0; Fig. 4b) (Wones and Eugster 1965), consistent with similar estimates from Johnson et al. (2015), Johnson (2020), and Olson (2022) for the nearby Emigrant Pass volcanic field. No titanite was observed in any samples, which also suggests that most samples equilibrated at <ΔNNO+2 (Wones 1989).

Rayleigh fractional crystallization modeling

We assume fractional crystallization is a key mechanism in the evolution of the melts we observe trapped in quartz given their highly evolved character and their relatively low crystal cargo (dikes contain ~11–27% crystals, rhyolite dome ~20% crystals, Caetano Tuff contains ~38–40% crystals, and post-caldera plutons contain ~40–61% crystals, Table 1). Simple Rayleigh fractional crystallization modeling of incompatible elements (without assimilation or recharge, details in Online

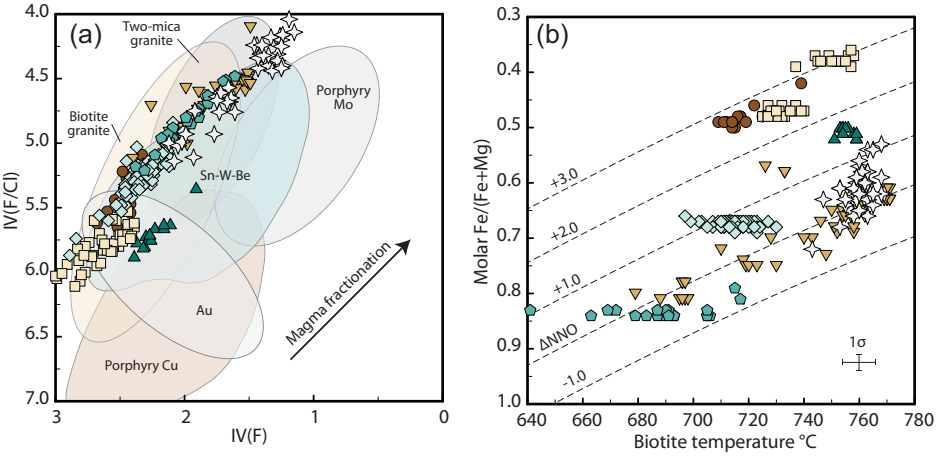

Figure 4. Biotite compositions. (**a**) F and Cl intercept values, IV(F) and IV(Cl) (Munoz 1984). Biotite compositions genetically associated with various granite and ore deposit types are shown for reference (Jin et al. 2018; Zhang et al. 2016; Munoz 1984). (**b**) Biotite Fe/Mg compositions [molar Fe/(Fe+Mg)] and calculated biotite temperatures (Henry et al. 2005) are shown with corresponding estimates for sample oxygen fugacity (Wones and Eugster 1965). Error bars show estimated 1σ uncertainties based on multiple analyses and the estimated uncertainty in the X_{Mg}-Ti-in-biotite thermometer of Henry et al. (2005). Sample symbols are the same as in Figures 2 and 3.

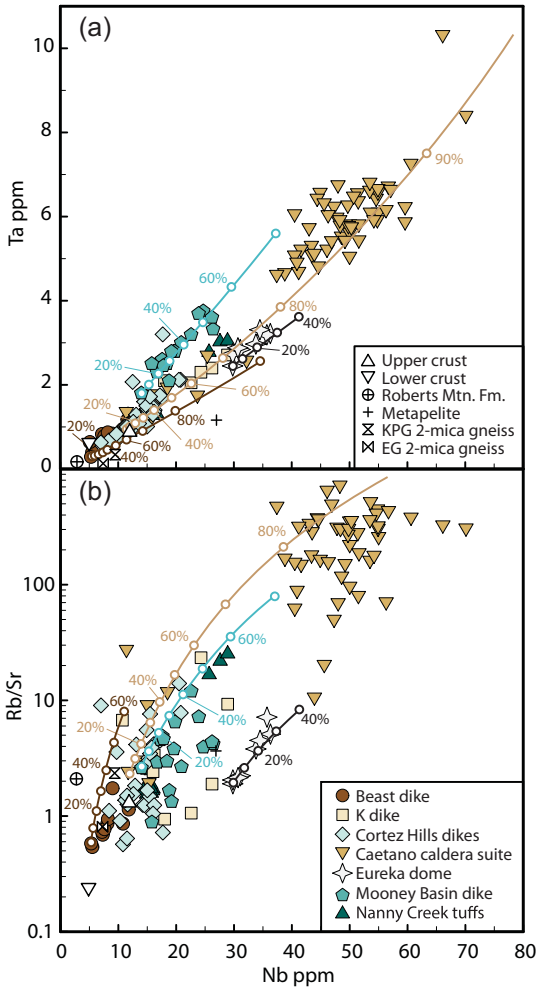

Figure 5. Rayleigh fractional crystallization modeling results. (**a**) Ta vs. Nb, both of which are highly incompatible. (**b**) Rb/Sr ratio vs. Nb highlights the diversity of feldspar fractionation within each volcanic center. Model lines show 10% crystallization increments. Estimated 1σ uncertainties are smaller than symbols. Values of the average upper crust, lower crust, black calcareous mudstones of the Roberts Mountains Formation (Mtn. Fm.), miogeoclinal metapelites of the McCoy Creek Group, and two-mica granitic gneiss are the same as in Figure 2. Also shown is a two-mica granitic gneiss from the northern Ruby Mountains metamorphic core complex, representing mid-crustal, anatectic granites (EG = equigranular two-mica granitic gneiss formed by biotite dehydration) (Lee et al. 2003).

Materials[1] Appendix 1.10), starting with the least evolved melt for each volcanic center, suggests that the spectrum of observed melts represent a broad window of melt evolution (e.g., 5–70 ppm Nb, 0.3–10 ppm Ta, 0.5–700 Sr/Rb; Fig. 5). Each volcanic center displays a somewhat different lineage, with compositionally distinct starting melts evolving with slightly different sloping trends controlled by distinctive minor and accessory phase proportions. Melts from the Beast dike show the least amount of overall evolution (i.e., melts were trapped after ~30–40% crystallization of the least evolved melt), followed by those from the Mooney Basin dike (~50% crystallization). In contrast, melts from the Cortez Hills dikes and the Caetano caldera suite display the highest degree of melt evolution, with the span between the least evolved melt and most evolved melts requiring trapping after up to ~80% (Mercer 2021) and ~90% crystallization, respectively, presumably requiring a crystal separation process like filter pressing. For the Caetano caldera suite, this is consistent with EC-RAxFC modeling of whole rock data (Watts et al. 2016), suggesting up to >80% crystallization. They also display the most scatter among incompatible elements, probably due to the incorporation of large amounts of variable crustal components affecting trace element contents (Watts et al. 2016). The Eureka dome magma appears to have tapped an already more evolved melt source (starting melt ~30 ppm Nb), though inclusions show less overall melt evolution for this volcanic center (~30–35% crystallization).

Discussion

Characteristics of "suspect" rhyolites

As we set out to characterize the "suspect" magmas in Carlin-type ore-forming systems, we expected to identify magmas of a particular "flavor" characteristic of the tectonic setting over the relatively narrow ~7 m.y. snapshot of time; allowing perhaps for some differences between magmas that traversed different lithospheric domains (e.g., Proterozoic lithosphere to the east and transitional accreted lithosphere to the west, Fig. 1). However, the broad compositional spectrum of rhyolites exhibited by these data suggest a more complex picture of silicic crustal magmatism operating across the region over a narrow span of time during slab rollback; with no immediately obvious correlation with lithospheric domain (i.e., in the absence of isotopic data, a possible future research direction).

On one end of the compositional spectrum are rhyolites that, for simplicity, we refer to as having I-type affinity (e.g., Chappell et al. 2012). Melts from the Beast dike probably best exemplify this end-member (in the western lithospheric domain). These melts tend to (1) extend from calc-alkaline to high-K calc-alkaline series (Fig. 2a); (2) have Eu anomalies that are small to non-existent suggesting relatively little plagioclase fractionation (Fig. 2c); (3) have lower overall Y+Nb (Fig. 2d); (4) trend toward higher Sr/Y and La/Yb values (in some cases, reaching "adakitic" values; Figs. 2e and 2f); (5) be H_2O-rich relative to their extent of evolution (i.e., high H_2O/Nb; Online Materials[1] Appendix 3.3); (6) contain biotite indicative of more oxidized conditions ($f_{O_2} > \Delta NNO + 1$; Fig. 4b); and (7) tend to be relatively less fractionated in general (Fig. 5). Other magmatic centers displaying some of these characteristics include the Nanny Creek tuff (in the eastern lithsopheric domain, especially the older unit) and the K and Cortez Hills dikes (in the western lithospheric domain). In the context of subduction-related I-type magma characteristics, "adakitic" signatures in mid- to upper crustal silicic magmas are significant. Intermediate-depth and shallowly evolving silicic magmas precipitate early and abundant plagioclase, which depletes the residual melt in Sr and Eu while accumulating Y and Yb. Thus, at intermediate to shallow depths (700–300 MPa), non-adakitic calc-alkalic signatures are typical (Loucks 2021). In contrast, hydrous mafic magmas evolving at higher pressures precipitate early and plentiful

hornblende, which depletes the melt in Y and Yb while Sr and Eu accumulate in the residual melt until it cools enough for plagioclase to saturate. At deeper levels where garnet is stable, equilibrating melts develop even larger Y and HREE depletions. Therefore, "adakitic" signatures suggest incorporation of melts from long-lived, intermittently replenished, deep magma reservoirs in MOHO-vicinity stress traps upon relaxation of geodynamic stress (Richards and Kerrich 2007; Richards 2011; Chiaradia et al. 2012; Castillo 2012; Richards et al. 2012; Chiaradia 2015; Loucks 2021). While no true adakites (i.e., subducting slab melts) (Defant and Drummond 1990) have been documented in this region (Best et al. 2009), many Eocene intrusions in Nevada range to Sr/Y > 20 and Y < 18 ppm (Fig. 2e) (du Bray 2007). Interestingly, three of the four samples with the strongest "adakitic" signatures longitudinally parallel a postulated slab tear, which may have created conditions permissive of true adakite generation (Fig. 1) (Best et al. 2016; Thorkelson and Breitsprecher 2005; Eyuboglu et al. 2013). This topic may warrant further investigation and could have interesting implications on metallogenesis in this region. Despite these I-type characteristics, melts on this end of the spectrum are notably weakly to strongly peraluminous (Fig. 2b), presumably inherited from moderate contributions from mid- to upper-crustal aluminous lithologies as magmas evolved and ascended. Magmatic systems with I-type affinity, especially adakitic melts, are typically endowed with higher H_2O and SO_3 concentrations and are typically associated with porphyry Cu-Mo-W-Au-Ag mineralization and related deposits (Ishihara 1981; Černý et al. 2005; Hofstra and Kreiner 2020; Loucks 2021; Vikre et al. 2023).

On the other end of the spectrum are rhyolites that, for simplicity, we refer to as having A-type affinity (e.g., Bonin 2007; Frost and Frost 2011). The melts represented in the Caetano caldera suite best illustrate this end-member (in the western lithospheric domain). Melts from this end of the spectrum tend to: (1) range from high-K calc-alkaline to shoshonite series (Fig. 2a); (2) have flatter REE patterns with more pronounced negative Eu anomalies characteristic of more highly evolved, feldspar-fractionated magmas (Fig. 2c); (3) contain overall higher Y+Nb values (Fig. 2d); (4) have lower Sr/Y and La/Yb values (Figs. 2e and 2f); (5) be relatively H_2O-poor relative to their extent of evolution (i.e., lower H_2O/Nb; Online Materials[1] Appendix 3.3); (6) contain biotite indicative of more reducing conditions and containing higher F contents ($f_{O_2} < \Delta NNO + 1$; up to several wt% F; Fig. 4b; Online Materials1 Appendix 3.5); and (7) tend to be more F-rich and highly fractionated (up to ~8000 ppm F; Fig. 5). Magmatic centers that share some of these traits include the Eureka dome and Mooney Basin dike (eastern lithospheric domain). In the context of A-type (or more specifically, "ferroan") (Frost and Frost 2011) magma characteristics, F-rich magmas are a subtype classically associated with post-subduction, continental rift settings with thick cratonic crust (i.e., Climax-type systems and topaz rhyolites) (Sinclair 1995; Christiansen et al. 1983, 2007; Ludington and Plumlee 2009). It is thought that F may be sourced from preconditioning of the deep crust; either by previous biotite dehydration melting of the crust that leaves behind F-enriched, residual biotite (Skjerlie and Johnston 1992) or fluid-absent breakdown of amphibole in ultrahigh temperature lower crustal rocks during periods of unusually high heat flow (Rosera et al. 2023); both of which may enhance subsequent crustal melts with elevated fluorine. High degrees of magma fractionation tend to be associated with F-rich melts because, like H_2O, F depresses the melt solidus, thereby expanding crystallization *P-T* conditions (Webster et al. 1987) and depressing melt viscosity (e.g., Giordano et al. 2004; Mercer et al. 2015). The most A-type melts in this study tend to contain the highest melt F contents and the most halogen-enriched biotite compositions (Fig. 4). They also display the most highly evolved melt compositional arrays (Fig. 5). While most of the A-type samples in this study do not attain the extreme concentrations of F or incompatible elements of highly evolved topaz rhyolites (e.g., Nb, Rb, HREEs; Figs. 2d and 4a), the most evolved melts from the Caetano caldera suite do (e.g., Caetano caldera suite ~10–70 ppm Nb; topaz rhyolites of the western U.S.A. ~14–280 ppm Nb). Rhyolites with A-type affinity range from barely metaluminous to strongly peraluminous (Fig. 2b), apparently indicating some strong interactions with aluminous crustal lithologies during magma evolution and ascent. In the case of the Caetano Tuff, it is one of the most ^{18}O-enriched rhyolites in all of Nevada ($\delta^{18}O = 10.2 \pm 0.2‰$; Watts et al. 2016), which indicates significant anatexis of metasedimentary crustal rocks. The resurgent Carico Lake pluton within the Caetano caldera contains abundant mafic metapelitic, hyperaluminous xenoliths (ASI = 1.5 to 2.8, Fig. 2b) (Watts et al. 2016). Modeling of Sr and Nd isotopes by Watts et al. (2016) suggests that the Caetano caldera suite magmas incorporated ~70–80% crustal material and only 20–30% mantle-derived basalt. Our petrogenetic observations above are consistent with these isotopic data. Highly evolved A-type magmatic systems are typically endowed with incompatible elements and associated with Mo-W-Sn mineralized systems (Ishihara 1981; Lehmann 1982; Černý et al. 2005; Hofstra and Kreiner 2020; Cheng et al. 2018).

Melts from the Nanny Creek tuff display the best example of a hybrid magmatic system. These melts exhibit a moderate oxidation state (Fig. 4b) and show distinct similarities to melts from both the Beast dike and Caetano caldera suite end-members. Despite this spectrum of compositions, the rhyolitic systems in this study do have two things in common—they are all consistently ferroan [FeO/(FeO+MgO) > 0.85] and are generally peraluminous (ranging to high ASI values in both melts and biotite; Fig. 2b; Online Materials[1] Appendix 2). This is most likely an expression of the relatively elevated crustal geotherm at the time giving rise to more Fe-rich compositions (Best et al. 2016) and/or a result of dehydration melting of crustal I-type granite source rocks (at pressures below garnet stability; Chappell et al. 2012) and/or some degree of incorporation of highly peraluminous metasedimentary rocks that exist in either lithospheric domain (Clarke 2019). An elevated geotherm requires higher than usual oxidation states to stabilize and fractionate Fe-Ti oxides (Ghiorso and Evans 2008), leading to the development of more Fe-rich magmas. Eocene intrusions across northern Nevada also reflect this ferroan character, and a large number of Jurassic to Tertiary intrusions across the region are known to be peraluminous, ~20% of which are moderately to strongly peraluminous or hyperaluminous (du Bray 2007; Fig. 2b; Online Materials[1] Appendix 3.1). Among many proposed mechanisms

for generating strongly peraluminous magmas, contamination by pelitic crustal material (ASI > 1.5) is highly effective (Clarke 2019). Incorporation of metasedimentary basement rocks similar to the Neoproterozoic McCoy Group (fault-stacked shelf sediments including mica schists, phyllites, argillites, metasiltstones, and quartzites) has been suggested in the petrogenesis of peraluminous granites of Lamoille Canyon (located between the Carlin and Long Canyon Trends; Lee et al. 2003) as well as rhyolites of the Caetano Tuff (Watts et al. 2016). These lithologies may be important in the evolution of several of the rhyolites in this study.

Constraints on crustal magma reservoir conditions

A synthesis of barometry, volatile elements, thermodynamic and trace element modeling, and crystallinity information can help to put constraints on magma reservoir conditions in these magmatic systems. The deepest-trapped quartz-hosted melt inclusions within each volcanic center occur largely between ~7–12 km, within the brittle-ductile transition zone (Fig. 6). These entrapment depths probably indicate the lower levels of upper crustal magma reservoirs for these centers. This crustal region is where ascending melts are expected to stall in the crust because the stress required to fracture the brittle crust increases by two orders of magnitude here (Vigneresse 1995). It largely coincides with the depths of fluid-saturated plutons hypothesized to be related to Carlin-type Au deposits (~6–12 km) (Muntean et al. 2011; Henry et al. 2020, 2023). At the top of the brittle-ductile transition zone (~7–8 km), the most H_2O-rich magmas (Caetano caldera suite, Cortez Hills, Mooney Basin, Beast, and K dikes; Fig. 3) appear to reach fluid saturation (blue shaded rectangles, Fig. 6). Most of the quartz-hosted melt inclusions analyzed were trapped a bit shallower (~3–7 km), probably indicating a well-developed network of shallower, interconnected, polybaric magma reservoirs and/or conduits residing largely as crystal mushes where magmas continued to exsolve fluids and crystallize (Cashman and Giordano 2014; Bachmann and Huber 2016; Sparks et al. 2019; Cashman and Edmonds 2019). The driest magmatic centers (Eureka dome, Nanny Creek tuffs) appear to have ascended largely under fluid-undersaturated conditions, with the Eureka dome magma perhaps reaching fluid saturation at shallower depths of ~3–4 km. At even shallower levels (<3 km), magmas from the Caetano caldera suite and Cortez Hills dikes appear to have continued significant quartz crystallization and degassing upon final ascent to the surface, potentially indicating ascent slow enough to support significant quartz crystallization and inclusion entrapment. In contrast, magmas from the Beast and K dikes, Eureka dome, and Nanny Creek tuff appear to have ceased quartz-hosted melt inclusion entrapment at these shallow depths, plausibly indicating rapid ascent that prohibited significant quartz phenocryst growth (but permissive of microlite growth) on route to the surface.

The crystallinities observed in hand samples (Table 1) are notably lower than the extent of crystallization necessary to create the spectrum of trace elements we observe in quartz-hosted inclusions (Fig. 5) (Mercer 2021). For example, Beast, Cortez Hills, and Mooney Basin dike hand samples contain ~11–27% crystals, and the Eureka dome sample contains ~20% crystals, but trace element modeling indicates entrapment spanning ~30–40% (Beast dike), ~80% (Cortez Hills dikes), ~50% (Mooney Basin dike), and ~30–35% crystallization (Eureka dome). The Caetano Tuff samples contain ~38–40% crystals, and the post-caldera pluton samples contain ~40–61% crystals, whereas trace element modeling suggests up to ~90% crystallization. This discrepancy is probably best explained by a mechanism, such as filter pressing and/or remobilization by mafic underplating and/or CO_2 sparging (Bachmann and Bergantz 2006; Caricchi et al. 2018), required to facilitate melt segregation events. This was also suggested by EC-RAxFC modeling of whole rocks for the most evolved samples from the Caetano caldera suite (Watts et al. 2016). The observed crystallinities in dikes, domes, and tuffs are within theoretical crystallinities for eruptible magma pockets (<40–50%; Cooper and Kent 2014), whereas those in the post-caldera plutons are consistent with nearly immobile crystal mushes (>40–50% crystals).

The broad spectrum of rhyolite characteristics exhibited by the "suspect" magmatic systems traversing both eastern and western lithospheric domains over ~7 m.y. suggests varied evolutionary pathways as magmas ascended through the crust, mobilizing magmas from different reservoirs with distinct characteristics. This is consistent with current models of ignimbrite flare-up magmatism (e.g., de Silva and Gosnold 2007; de Silva 2008; Loucks 2021), complex silicic magma reservoirs (Cashman and Giordano 2014; Bachmann and Huber 2016; Sparks et al. 2019), and mobilization of melt-rich pockets within crystal mushes (e.g., Bachmann and Bergantz 2008). The ignimbrite flare-up in northern Nevada was preceded by long-lived, contractional deformation in the region (Dickinson 2006; Best et al. 2016). Under these conditions, typical orogenic horizontal deviatoric stress values (~10–30 MPa) exceed magmatic buoyancy forces that drive magma ascent, thereby trapping kilometer-thick zones of buoyant magmas at all crustal depths down to the MOHO (Loucks 2021). These stress-trapped magmas are essentially thermally "immortal" and can differentiate significantly to granitoid compositions as long as compressive stresses last >5–10 m.y. and mafic replenishment occurs from the mantle (Loucks 2021). Upon slab rollback and waning of compressive stresses, an increase in mantle-derived magma flux and associated heat transfer by advection, conduction, and/or CO_2 sparging (Bachmann and Bergantz 2006; Caricchi et al. 2018) at the MOHO would have mobilized stress-trapped reservoirs. Crustal relaxation propagating from the shallow crust downward, could have successively rejuvenated stress-trapped magma reservoirs, with those from the deep crust sourcing F-enriched magmas (Rosera et al. 2023) and those from the MOHO-vicinity sourcing "adakitic" magmas (Loucks 2021).

Within this framework, Eocene rhyolite systems in northern Nevada do not appear to reflect evolution within a simple crustal reservoir but are instead the result of the complex interconnection of crustal reservoirs. They apparently tapped mobile pockets from a diverse array of magma reservoirs from the MOHO to the upper crust during slab rollback and high heat flux that ostensibly drove the ignimbrite flare-up. That Carlin-type Au systems appear to be associated with a broad compositional spectrum of silicic magmatic systems is perhaps no surprise given their as yet enigmatic and unclear petrogenetic signature.

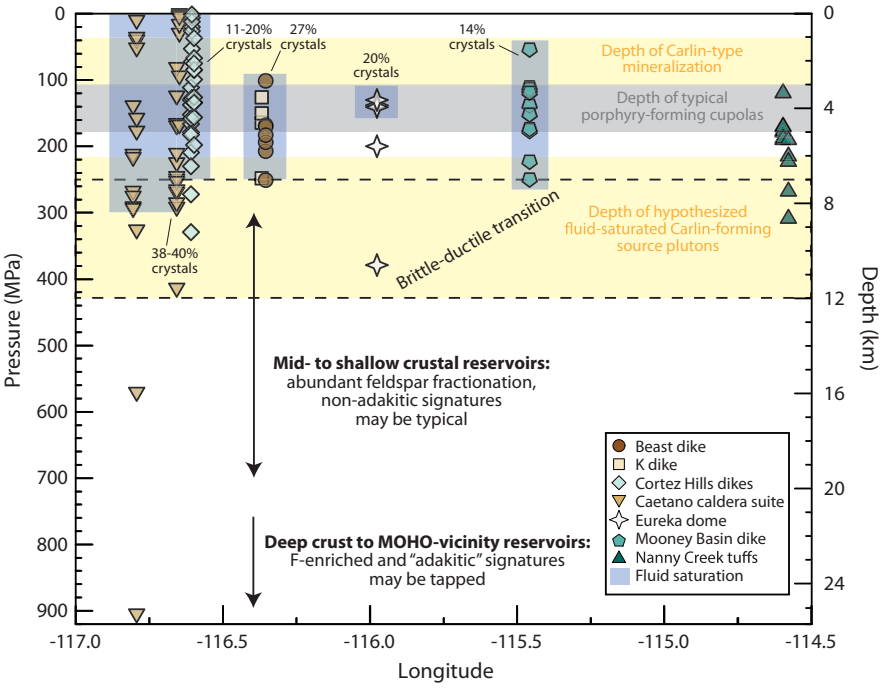

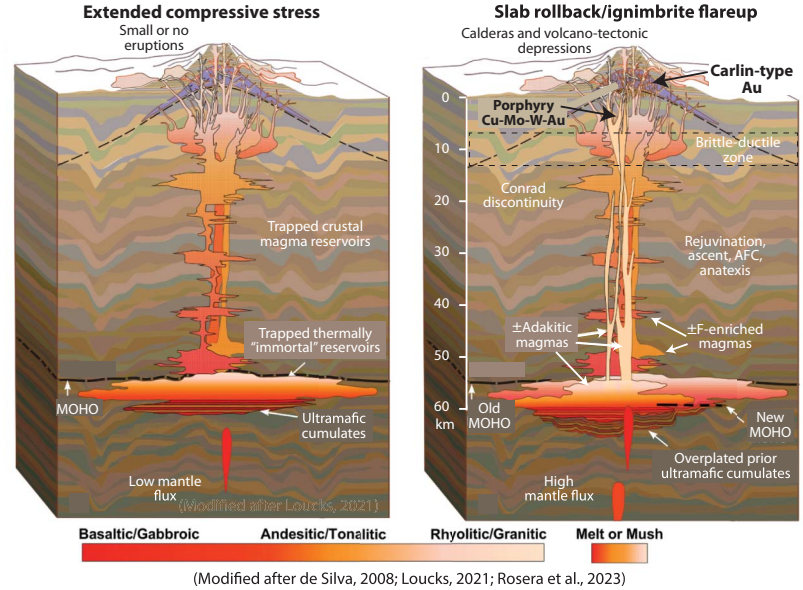

(Modified after de Silva, 2008; Loucks, 2021; Rosera et al., 2023)

Figure 6. Magma reservoir constraints. (**top**) Calculated entrapment depths of quartz-hosted melt inclusions from each magmatic center, from west to east. Blue highlighted areas show fluid saturation depths for each magmatic center inferred from volatile data and Rhyolite-MELTS modeling. Estimated 1σ uncertainties are about the size of the symbols. (**bottom**) Schematic cross section of magma reservoirs transitioning from post-subduction, long-lived contractional deformation to slab rollback and associated crustal relaxation and ignimbrite flare-up (modified after de Silva 2008; Loucks 2021; Rosera et al. 2023). Scale is approximate for thick crust (~40–70 km) (Best et al. 2009; Snee and Miller 2022).

Implications

The key trace element characteristics distinguishing these magmatic centers are summarized in an 11-component radar spider diagram (Fig. 7). The center of the diagram represents the origin, and each axis extends to the maximum unit (or 100% relative) for each component, with contours representing 10% relative increments. The broad spectrum of rhyolite characteristics of these "suspect" Eocene magmatic systems contemporaneous with nearby Carlin-type Au mineralization is surprising, although perhaps not unexpected given the geodynamics at the time.

As the Farallon slab rolled back beneath the region, the tectonic regime transitioned from post-subduction, long-lived contractional deformation of the Nevadaplano to crustal relaxation and ensuing arc-style ignimbrite flare-up magmatism that swept across the region, later developing into full-blown classic Basin and Range bimodal extensional magmatism (Best et al. 2016). Dramatic changes in magma characteristics have been documented isotopically by Cousens et al. (2019) in igneous rocks from the Fish Creek Mountains, further west of our field sites. There, igneous rocks spanning from ~40 to ~1 Ma highlight the drastic transition from slab rollback and ignimbrite flare-up to rifting. While the magmatic centers in our study encompass a much

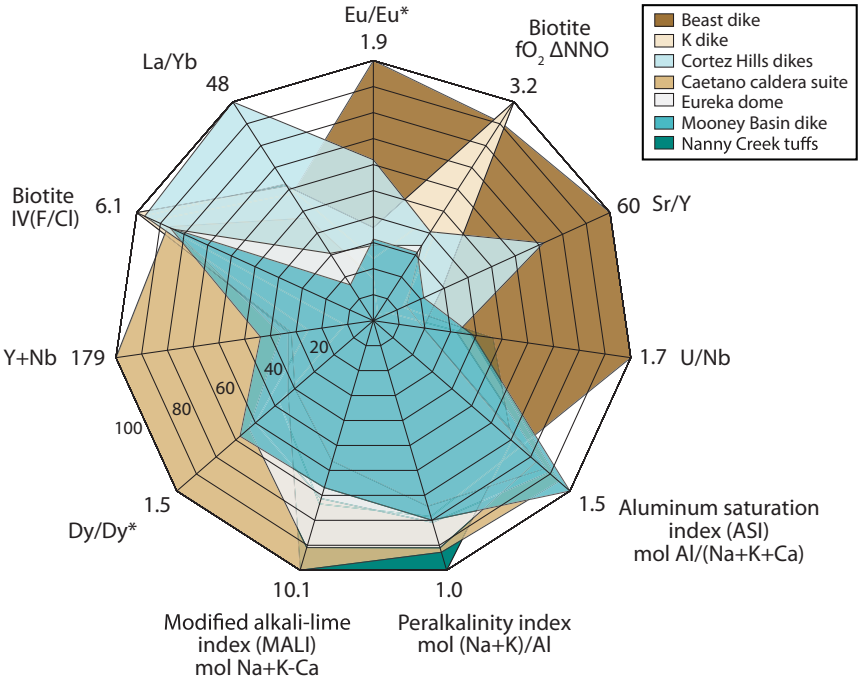

Figure 7. Radar spider diagram showing key compositional characteristics for magmatic centers. The general interpretation of these variables is as follows (see text for more details): Eu/Eu* = indicator of melt evolution by plagioclase fractionation; biotite f_{O_2} ΔNNO = estimate of magma redox relative to the nickel-nickel oxide buffer; Sr/Y = indicator of melts that equilibrated near the MOHO with amphibole (±garnet); U/Nb = anomalous trace element enrichment possibly indicating small degree partial melt of sediments and/or brine contributions to the magmas; aluminum saturation index (ASI) = variable used to classify feldspathic igneous rocks, separating metaluminous from peraluminous compositions; peralkalinity index = variable used in feldspathic igneous rock classification, discriminating peralkaline rocks from metaluminous and peraluminous rocks; modified alkali-lime index (MALI) = variable used to classify feldspathic igneous rocks, a measure of calcic to alkalic affinity; Dy/Dy* = a measure of the curvature of REE patterns, highlighting melt contributions controlled by mid- to deep-crustal phases such as amphibole/clinopyroxene and garnet, and source LREE-depletion or LREE enrichment; Y+Nb (ppm) = incompatible elements used to discriminate I-type rhyolites from A-type rhyolites; biotite IV(F/Cl) = indicator of halogen activity in the magma, corrected for Mg/Fe ratio in the biotite, with lower values associated with higher degrees of F enrichment; La/Yb = measure of the enrichment of LREE over HREE and melts that equilibrated near the MOHO with amphibole (±garnet).

shorter timeframe than in the Fish Creek Mountains, they appear to show various distinct magma characteristics reflecting the dynamic tectonic-magmatic setting during Eocene crustal relaxation and associated complex interactions among diverse crustal magma reservoirs.

In addition to sourcing magmas from diverse reservoirs, we speculate that there could be additional magma evolution processes adding to the diversity of rhyolite characteristics. For example, melts from the Beast dike exhibit unique trace element enrichments in Li, B, Al, Cl, V, Se, Bi, and U (Online Materials[1] Appendix 3.6), possibly due to incorporation of small degree partial melts of strata such as marine shales or limestones (Al, Li, B, Bi, U; Chan et al. 2006), carbonaceous black shales (V, Se, Au, As, Sb, Mo, Cu, Ag, Pb, Ni, Te) (Emsbo et al. 2006; Large et al. 2011), and/or brines (Li, B, Cl, U) (Seward et al. 2014). Identifying such enrichments is significant because these components could provide additional ore metals. Interestingly, the Caetano caldera suite—one of Nevada's most ^{18}O-enriched rhyolites owing to significant (~70–80%) anatectic melt from pelitic, metasedimentary basement rocks (Watts et al. 2016)—does not show such trace element enrichments. This may be explained by Caetano suite magmas hybridizing larger degree partial melts that effectively dilute such distinctive trace element signatures. Notably, the enrichments in melts from the Beast dike, and to some extent other I-type melts (e.g., Cortez Hills dikes), show a positive correlation with Sr/Y. This may suggest derivation by subducting slab components (B, Cl, U) (Edwards et al. 1993) and/or pelagic sediment (Li) (Walker et al. 2009). Rare earth element pattern curvature analysis [Dy/Dy*, Dy/Yb (Davidson et al. 2013) Online Materials[1] Appendix 3.7] supports this supposition. We highlight these interesting trace element features as a potential focus for future work leveraging isotopic discrimination of such processes (e.g., fingerprinting black shales using molybdenum isotopes) (Xue et al. 2023) that could advance our understanding of magmatism and metallogenesis in this region.

The resultant silicic magmatic spectrum featured in our sample suite encompasses a range of mineralization associations (Hofstra and Kreiner 2020) consistent with the prolific and diverse array of ore deposits that formed during this time, including subduction-related porphyry/skarn Cu-Mo-W-Au, epithermal Ag-Au deposits, and distal disseminated Ag-Au deposits found across this region. In addition, some post-subduction, thick-crust extensional rare-metal mineralizing systems endowed with Mo(Sn-W-F-Be-Ag-Au) have also been recognized across the region during the middle to late Cenozoic (e.g., Mt. Hope porphyry

Mo-Cu- Ag-Au deposit, 38–36 Ma) (Ludington and Plumlee 2009). Carlin-type Au deposition appears to be associated with nearly the entire ~7 m.y. silicic magma spectrum, bracketed by the most I-type system (i.e., Beast dike) pre-dating mineralization and the most evolved A-type system (i.e., Caetano caldera suite) post-dating mineralization. The evident indifference of Carlin-type Au systems to a specific silicic magma "flavor" seems to imply that if magmas are involved in their genesis, they perhaps do not need to be compositionally specialized. Perhaps the magmatic-hydrothermal systems that are clearly circulating and intertwined with some Carlin-type Au systems (e.g., Cortez Hills; Mercer 2021) are only relevant as heat sources driving circulation of hydrothermal fluids to remobilize and redistribute metals already residing in the host rocks. As such, perhaps they may perform this function both proximally and distally, giving rise to the disparity of field, geochemical, geophysical, and thermobarometric evidence for specialized causal intrusions.

Acknowledgments and Funding

We thank R. Becker of Newmont Mining Corporation and R. Bond, M. McMullen, P. Anderson, and M. Bardou of Barrick Gold Corporation for sharing their enthusiasm in the field and expertise in the region. We also thank Z. Zajacz, A. Tsay, C. Grondahl, and T. Todorov for support with laser ablation analyses and data reduction, and M. Coble for support with SHRIMP-RG analyses and data reduction. Thank you to C.M. Mercer for help plotting data in Python and M.A. Mercer and G. Arrieta for thoughtful geologic and technique discussions. We are immensely grateful for the time and valuable feedback we received from editors and reviewers including R. Orndorff, A. Acosta-Vigil, R. Esposito, D. Coleman, M. Williams, D. John, M. Myers, E. Christiansen, J. Cline, A. Pamukcu, Z. Zajacz, A. Tsay, and two anonymous reviewers. Any use of trade, firm, or product names is for descriptive purposes only and does not imply endorsement by the U.S. Government.

References Cited

Acosta-Vigil, A., London, D., Morgan, G.B., and Dewers, T.A. (2003) Solubility of excess alumina in hydrous granitic melts in equilibrium with peraluminous minerals at 700–800 °C and 200 MPa, and applications of the aluminum saturation index. Contributions to Mineralogy and Petrology, 146, 100–119, https://doi.org/10.1007/s00410-003-0486-6.

Arbonies, D.G., Creel, K.D., Jackson, M.L., Steininger, R., and Pennell, B. (2011) Cortez Hills lower zone discovery and geologic update. Great Basin evolution and metallogeny, 447–462.

Audétat, A. and Simon, A. (2012) Magmatic controls on porphyry copper deposits. Society of Economic Geologists Special Publication, 16, 553–572.

Bachmann, O. and Bergantz, G.W. (2006) Gas percolation in upper-crustal silicic crystal mushes as a mechanism for upward heat advection and rejuvenation of near-solidus magma bodies. Journal of Volcanology and Geothermal Research, 149, 85–102, https://doi.org/10.1016/j.jvolgeores.2005.06.002.

——— (2008) Rhyolites and their source mushes across tectonic settings. Journal of Petrology, 49, 2277–2285, https://doi.org/10.1093/petrology/egn068.

Bachmann, O. and Huber, C. (2016) Silicic magma reservoirs in the Earth's crust. American Mineralogist, 101, 2377–2404, https://doi.org/10.2138/am-2016-5675.

Barnes, C.G., Burton, B.R., Burling, T.C., Wright, J.E., and Karlsson, H.R. (2001) Petrology and geochemistry of the late Eocene Harrison Pass pluton, Ruby Mountains core complex, northeastern Nevada. Journal of Petrology, 42, 901–929, https://doi.org/10.1093/petrology/42.5.901.

Barton, M.D. (1996) Granitic magmatism and metallogeny of southwestern North America. Earth and Environmental Science Transactions of the Royal Society of Edinburgh, 87, 261–280, https://doi.org/10.1017/S0263593300006672.

Best, M.G., Barr, D.L., Christiansen, E.H., Gromme, S., Deino, A.L., and Tingey, D.G. (2009) The Great Basin Altiplano during the middle Cenozoic ignimbrite flare-up: Insights from volcanic rocks. International Geology Review, 51, 589–633, https://doi.org/10.1080/00206810902867690.

Best, M.G., Christiansen, E.H., de Silva, S., and Lipman, P.W. (2016) Slab-rollback ignimbrite flare-ups in the southern Great Basin and other Cenozoic American arcs: A distinct style of arc volcanism. Geosphere, 12, 1097–1135, https://doi.org/10.1130/GES01285.1.

Boehnke, P., Watson, E.B., Trail, D., Harrison, T.M., and Schmitt, A.K. (2013) Zircon saturation re-revisited. Chemical Geology, 351, 324–334, https://doi.org/10.1016/j.chemgeo.2013.05.028.

Bonin, B. (2007) A-type granites and related rocks; evolution of a concept, problems and prospects. Lithos, 97, 1–29, https://doi.org/10.1016/j.lithos.2006.12.007.

Brooks, W.E., Thorman, C.H., and Snee, L.W. (1995) The $^{40}Ar/^{39}Ar$ ages and tectonic setting of the middle Eocene northeast Nevada volcanic field. Journal of Geophysical Research: Solid Earth, 100, 10403–10416, https://doi.org/10.1029/94JB03389.

Butters, D., Blundy, J., Tattitch, B., and Hawkesworth, C. (2025) Transcrustal, volatile-charged silicic melts revealed by zircon-hosted melt inclusions. Earth and Planetary Science Letters, 655, 119252, https://doi.org/10.1016/j.epsl.2025.119252.

Caricchi, L., Sheldrake, T.E., and Blundy, J. (2018) Modulation of magmatic processes by CO_2 flushing. Earth and Planetary Science Letters, 491, 160–171, https://doi.org/10.1016/j.epsl.2018.03.042.

Cashman, K.V. and Edmonds, M. (2019) Mafic glass compositions: A record of magma storage conditions, mixing and ascent. Philosophical Transactions of the Royal Society A, 377, 20180004, https://doi.org/10.1098/rsta.2018.0004.

Cashman, K.V. and Giordano, G. (2014) Calderas and magma reservoirs. Journal of Volcanology and Geothermal Research, 288, 28–45, https://doi.org/10.1016/j.jvolgeores.2014.09.007.

Castellanos-Melendez, M.P., Dilles, J., Guillong, M., Bachmann, O., and Chelle-Michou, C. (2024) From birth to death: The role of upper-crustal thermal maturation and volcanism in porphyry ore formation revealed in the Yerington district. Earth and Planetary Science Letters, 647, 119053, https://doi.org/10.1016/j.epsl.2024.119053.

Castillo, P.R. (2012) Adakite petrogenesis. Lithos, 134-135, 304–316, https://doi.org/10.1016/j.lithos.2011.09.013.

Černý, P., Blevin, P.L., Cuney, M., and London, D. (2005) Granite-related ore deposits. Economic Geology 100th Anniversary Volume, 337–370.

Chakurian, A.M., Arehart, G.B., Donelick, R.A., Zhang, X., and Reiners, P.W. (2003) Timing constraints of gold mineralization along the Carlin trend utilizing apatite fission-track, $^{40}Ar/^{39}Ar$, and apatite (U-Th)/He methods. Economic Geology and the Bulletin of the Society of Economic Geologists, 98, 1159–1171, https://doi.org/10.2113/gsecongeo.98.6.1159.

Chan, L., Leeman, W.P., and Plank, T. (2006) Lithium isotopic composition of marine sediments. Geochemistry, Geophysics, Geosystems, 7, 1–25.

Chappell, B.W., Bryant, C.J., and Wyborn, D. (2012) Peraluminous I-type granites. Lithos, 153, 142–153, https://doi.org/10.1016/j.lithos.2012.07.008.

Cheng, Y., Spandler, C., Chang, Z., and Clarke, G. (2018) Volcanic-plutonic connections and metal fertility of highly evolved magma systems: A case study from the Herberton Sn-W-Mo Mineral Field, Queensland, Australia. Earth and Planetary Science Letters, 486, 84–93, https://doi.org/10.1016/j.epsl.2018.01.012.

Chiaradia, M. (2015) Crustal thickness control on Sr/Y signatures of recent arc magmas: An Earth scale perspective. Scientific Reports, 5, 8115, https://doi.org/10.1038/srep08115.

Chiaradia, M., Ulianov, A., Kouzmanov, K., and Beate, B. (2012) Why large porphyry Cu deposits like high Sr/Y magmas? Scientific Reports, 2, 685, https://doi.org/10.1038/srep00685.

Christiansen, E.H., Burt, D.M., Sheridan, M.F., and Wilson, R.T. (1983) The petrogenesis of topaz rhyolites from the western United States. Contributions to Mineralogy and Petrology, 83, 16–30, https://doi.org/10.1007/BF00373075.

Christiansen, E.H., Sheridan, M.F., and Burt, D.M. (1986) The Geology and Geochemistry of Cenozoic Topaz Rhyolites from the Western United States. Geological Society of America, Special Papers, Volume 205.

Christiansen, E.H., Baxter, N., Ward, T.P., Zobell, E., Chandler, M.R., Dorais, M.J., Kowallis, B.J., and Clark, D.L. (2007) Cenozoic Soldiers Pass volcanic field, central Utah—Implications for the transition to extension-related magmatism in the Basin and Range Province. Utah Geological Survey Publication, 36, 123–142.

Clarke, D.B. (2019) The origins of strongly peraluminous granitoid rocks. Canadian Mineralogist, 57, 529–550, https://doi.org/10.3749/canmin.1800075.

Cline, J.S. (2018) Nevada's Carlin-type gold deposits: What we've learned during the past 10 to 15 years. In J.L. Muntean, Ed., Diversity in Carlin-Style Gold Deposits, Volume 20, p. 7–37. Reviews in Economic Geology.

Cline, J.S., Hofstra, A.H., Muntean, J.L., Tosdal, R.M., and Hickey, K.A. (2005) Carlin-type gold deposits in Nevada: critical geologic characteristics and viable models. In J.W. Hedenquist, J.F.H. Thompson, R.J. Goldfarb, and J.P. Richards, Eds., Economic Geology 100th Anniversary. Volume 451–484. Society of Economic Geologists.

Colgan, J.P. and Henry, C.D. (2009) Rapid middle Miocene collapse of the Mesozoic orogenic plateau in north-central Nevada. International Geology Review, 51, 920–961, https://doi.org/10.1080/00206810903056731.

Colgan, J.P., Egger, A.E., John, D.A., Cousens, B., Fleck, R.J., and Henry, C.D. (2011) Oligocene and Miocene arc volcanism in northeastern California: Evidence for post-Eocene segmentation of the subducting Farallon plate. Geosphere, 7, 733–755, https://doi.org/10.1130/GES00650.1.

Cooper, K.M. and Kent, A.J. (2014) Rapid remobilization of magmatic crystals kept in cold storage. Nature, 506, 480–483, https://doi.org/10.1038/nature12991.

Cousens, B.L., Henry, C.D., Stevens, C., Varve, S., John, D.A., and Wetmore, S. (2019) Igneous rocks in the Fish Creek Mountains and environs, Battle

Mountain area, north-central Nevada: A microcosm of Cenozoic igneous activity in the northern Great Basin, Basin and Range Province, USA. Earth-Science Reviews, 192, 403–444, https://doi.org/10.1016/j.earscirev.2019.03.013.
Davidson, J., Turner, S., and Plank, T. (2013) Dy/Dy*: Variations arising from mantle sources and petrogenetic processes. Journal of Petrology, 54, 525–537, https://doi.org/10.1093/petrology/egs076.
de Silva, S.L. (2008) Arc magmatism, calderas, and supervolcanoes. Geology, 36, 671–672, https://doi.org/10.1130/focus082008.1.
de Silva, S.L. and Gosnold, W.D. (2007) Episodic construction of batholiths: Insights from the spatiotemporal development of an ignimbrite flare-up. Journal of Volcanology and Geothermal Research, 167, 320–335, https://doi.org/10.1016/j.jvolgeores.2007.07.015.
Defant, M.J. and Drummond, M.S. (1990) Derivation of some modern arc magmas by melting of young subducted lithosphere. Nature, 347, 662–665, https://doi.org/10.1038/347662a0.
Dickinson, W.R. (2006) Geotectonic evolution of the Great Basin. Geosphere, 2, 353–368, https://doi.org/10.1130/GES00054.1.
Dilles, P.A., Wright, W.A., Monteleone, S.E., Russel, K.D., Marlowe, K.E., Wood, R.A., and Margolis, J. (1996) The geology of the West Archimedes deposit: A new gold discovery in the Eureka mining district, Eureka County, Nevada. In A.R. Coyner and P.L. Fahey, Eds., Geology and Ore Deposits of the American Cordillera. Geological Society of Nevada Symposium, Reno, Proceedings, 159–171.
Dilles, J.H., Einaudi, M.T., Proffett, J., and Barton, M.D. (2000) Overview of the Yerington porphyry copper district: Magmatic to nonmagmatic sources of hydrothermal fluids, their flow paths, alteration affects on rocks, and Cu-Mo-Fe-Au ores.
Donovan, J.J., Lowers, H.A., and Rusk, B.G. (2011) Improved electron probe microanalysis of trace elements in quartz. American Mineralogist, 96, 274–282, https://doi.org/10.2138/am.2011.3631.
du Bray, E.A. (2007) Time, space, and composition relations among northern Nevada intrusive rocks and their metallogenic implications. Geosphere, 3, 381–405, https://doi.org/10.1130/GES00109.1.
Edwards, C.M.H., Morris, J.D., and Thirlwall, M.F. (1993) Separating mantle from slab signatures in arc lavas using B/Be and radiogenic isotope systematics. Nature, 362, 530–533, https://doi.org/10.1038/362530a0.
Ellis, B.S., Szymanowski, D., Magna, T., Neukampf, J., Dohmen, R., Bachmann, O., Ulmer, P., and Guillong, M. (2018) Post-eruptive mobility of lithium in volcanic rocks. Nature Communications, 9, 3228, https://doi.org/10.1038/s41467-018-05688-2.
Emsbo, P., Hutchinson, R.W., Hofstra, A.H., Volk, J.A., Bettles, K.H., Baschuk, G.J., and Johnson, C.A. (1999) Syngenetic Au on the Carlin trend: Implications for Carlin–type deposits. Geology, 27, 59–62, https://doi.org/10.1130/0091-7613(1999)027<0059:SAOTCT>2.3.CO;2.
Emsbo, P., Groves, D.I., Hofstra, A.H., and Bierlein, F. (2006) The giant Carlin gold province: A protracted interplay of orogenic, basinal, and hydrothermal processes above a lithospheric boundary. Mineralium Deposita, 41, 517–525, https://doi.org/10.1007/s00126-006-0085-3
Emsbo, P., McLaughlin, P.I., Breit, G.N., du Bray, E.A., and Koenig, A.E. (2015) Rare earth elements in sedimentary phosphate deposits: Solution to the global REE crisis? Gondwana Research, 27, 776–785, https://doi.org/10.1016/j.gr.2014.10.008.
Emsbo, P., McLaughlin, P.I., du Bray, E.A., Anderson, E.D., Vandenbroucke, T.R.A., and Zielinski, R.A. (2016) Rare earth elements in sedimentary phosphorite deposits—A global assessment. In P.L. Verplanck and M.W. Hitzman, Eds., Rare earth and critical elements in ore deposits. Reviews in economic geology, Volume 18, 101–114. Society of Economic Geologists, Inc.
Esposito, R. (2020) A protocol and review of methods to select, analyze and interpret melt inclusions to determine pre-eruptive volatile contents of magmas. In P. Lecumberri-Sanchez, M. Steele-MacInnis, and D. Kontak, Eds., Fluid and melt inclusions: Applications to Geologic Processes, 49. Mineralogical Association of Canada.
Esposito, R., Badescu, K., Steele-MacInnis, M., Cannatelli, C., De Vivo, B., Lima, A., Bodnar, R.J., and Manning, C.E. (2018) Magmatic evolution of the Campi Flegrei and Procida volcanic fields, Italy, based on interpretation of data from well-constrained melt inclusions. Earth-Science Reviews, 185, 325–356, https://doi.org/10.1016/j.earscirev.2018.06.003.
Esposito, R., Redi, D., Danyushevsky, L.V., Gurenko, A., De Vivo, B., Manning, C.E., Bodnar, R.J., Steele-MacInnis, M., and Frezzotti, M.L. (2023) Constraining the volatile evolution of mafic melts at Mt. Somma-Vesuvius, Italy, based on the composition of reheated melt inclusions and their olivine hosts. European Journal of Mineralogy, 35, 921–948, https://doi.org/10.5194/ejm-35-921-2023.
Eyuboglu, Y., Santosh, M., Dudas, F.O., Akaryalı, E., Chung, S., Akdağ, K., and Bektaş, O. (2013) The nature of transition from adakitic to non-adakitic magmatism in a slab window setting: A synthesis from the eastern Pontides, NE Turkey. Geoscience Frontiers, 4, 353–375, https://doi.org/10.1016/j.gsf.2012.10.001.
Farmer, M. (1996) An intrusive study of the Bluestar subdistrict: Carlin, Nevada. Newmont Gold Company, Internal report, 33 p
Fiedrich, A.M., Laurent, O., Heinrich, C.A., and Bachmann, O. (2020) Melt and fluid evolution in an upper-crustal magma reservoir, preserved by inclusions in juvenile clasts from the Kos Plateau Tuff, Aegean Arc, Greece. Geochimica et Cosmochimica Acta, 280, 237–262, https://doi.org/10.1016/j.gca.2020.03.038.
Frost, B.R. and Frost, C.D. (2008) A geochemical classification for feldspathic igneous rocks. Journal of Petrology, 49, 1955–1969, https://doi.org/10.1093/petrology/egn054.
Frost, C.D. and Frost, B.R. (2011) On ferroan (A-type) granitoids: Their compositional variability and modes of origin. Journal of Petrology, 52, 39–53, https://doi.org/10.1093/petrology/egq070.
Ghiorso, M.S. and Evans, B.W. (2008) Thermodynamics of rhombohedral oxide solid solutions and a revision of the Fe-Ti two-oxide geothermometer and oxygen-barometer. American Journal of Science, 308, 957–1039, https://doi.org/10.2475/09.2008.01.
Ghiorso, M.S. and Gualda, G.A.R. (2015) An H_2O–CO_2 mixed fluid saturation model compatible with Rhyolite-MELTS. Contributions to Mineralogy and Petrology, 169, 53, https://doi.org/10.1007/s00410-015-1141-8.
Giordano, D., Romano, C., Dingwell, D.B., Poe, B., and Behrens, H. (2004) The combined effects of water and fluorine on the viscosity of silicic magmas. Geochimica et Cosmochimica Acta, 68, 5159–5168, https://doi.org/10.1016/j.gca.2004.08.012.
Grauch, V.J.S., Rodriguez, B.D., and Wooden, J.L. (2003) Geophysical and isotopic constraints on crustal structure related to mineral trends in north-central Nevada and implications for tectonic history. Economic Geology and the Bulletin of the Society of Economic Geologists, 98, 269–286, https://doi.org/10.2113/98.2.269.
Gualda, G.A.R., Ghiorso, M.S., Lemons, R.V., and Carley, T.L. (2012) Rhyolite-MELTS: A modified calibration of MELTS optimized for silica-rich, fluid-bearing magmatic systems. Journal of Petrology, 53, 875–890, https://doi.org/10.1093/petrology/egr080.
Hastings, M.H. (2008) Relationship of base-metal skarn mineralization to Carlin-type gold mineralization at the Archimedes gold deposit, Eureka, Nevada. M.S. thesis, University of Nevada, Reno, 109 p.
Henry, C.D. and John, D.A. (2013) Magmatism, ash-flow tuffs, and calderas of the ignimbrite flare-up in the western Nevada volcanic field, Great Basin, USA. Geosphere, 9, 951–1008, https://doi.org/10.1130/GES00867.1.
Henry, D.J., Guidotti, C.V., and Thomson, J.A. (2005) The Ti-saturation surface for low-to-medium pressure metapelitic biotites: Implications for geothermometry and Ti-substitution mechanisms. American Mineralogist, 90, 316–328, https://doi.org/10.2138/am.2005.1498.
Henry, C.D., John, D.A., Heizler, M.T., Leonardson, R.W., Colgan, J.P., Watts, K.E., Ressel, M.A., and Cousens, B.L. (2020) Why did Great Basin Eocene magmatism generate Carlin-type gold deposits when extensive Jurassic to middle Miocene magmatism did not? Lessons from the Cortez region, northern Nevada, USA. In F.R. Koutz and W.M. Pennell, Eds., Vision for Discovery, Geological Society of Nevada 2020 Symposium Proceedings, Reno, 339–353. Geological Society of Nevada.
Henry, C.D., John, D.A., Leonardson, R.W., McIntosh, W.C., Heizler, M.T., Colgan, J.P., and Watts, K.E. (2023) Timing of Rhyolite Intrusion and Carlin-Type Gold Mineralization at the Cortez Hills Carlin-Type Deposit, Nevada, USA. Economic Geology and the Bulletin of the Society of Economic Geologists, 118, 57–91, https://doi.org/10.5382/econgeo.4976.
Hofstra, A.H. Critical minerals in Carlin-type systems of the United States. U.S. Geological Survey Scientific Investigations Report. (In press).
Hofstra, A.H. and Cline, J.S. (2000) Characteristics and models for Carlin-type gold deposits. Reviews in Economic Geology, 13, 163–220.
Hofstra, A.H. and Kreiner, D.C. (2020) Systems-deposits-commodities-critical minerals table for the Earth mapping resources initiative. U.S. Geological Survey Open-File Report 2020–1042, 24, https://doi.org/10.3133/ofr20201042.
Hofstra, A.H. and Wallace, A.R. (2006) Metallogeny of the Great Basin: Crustal evolution, fluid flow, and ore deposits. U.S. Geological Survey Open-File Report 2006–1280.
Hofstra, A.H., Snee, L.W., Rye, R.O., Folger, H.W., Phinisey, J.D., Loranger, R.J., Dahl, A.R., Naeser, C.W., Stein, H.J., and Lewchuk, M.T. (1999) Age constraints on Jerritt Canyon and other Carlin-type gold deposits in the western United States: Relationship to mid-Tertiary extension and magmatism. Economic Geology and the Bulletin of the Society of Economic Geologists, 94, 769–802, https://doi.org/10.2113/gsecongeo.94.6.769.
Hollingsworth, E.R. (2022) Characterization of Eocene paleogeography, magmatism, and ore deposition of the Piñon Range, Nevada: New insights into an integrated Carlin Gold deposit model, 460 p. Ph.D. thesis, University of Nevada.
Holm-Denoma, C.S., Hofstra, A.H., Rockwell, B.W., and Noble, P.J. (2017) The Valmy thrust sheet: A regional structure formed during the protracted assembly of the Roberts Mountains allochthon, Nevada, USA. Geological Society of America Bulletin, 129, 1521–1536, https://doi.org/10.1130/B31491.1.
Huang, R. and Audétat, A. (2012) The titanium-in-quartz (TitaniQ) thermobarometer: A critical examination and re-calibration. Geochimica et Cosmochimica Acta, 84, 75–89, https://doi.org/10.1016/j.gca.2012.01.009.
Humphreys, E.D. (1995) Post-Laramide removal of the Farallon slab, western United States. Geology, 23, 987–990, https://doi.org/10.1130/0091-7613(1995)023<0987:PLROTF>2.3.CO;2.

Ishihara, S. (1981) The granitoid series and mineralization. Economic Geology 75th Anniversary Volume, 458–484.
Jin, C., Gao, X.-Y., Chen, W.T., and Zhao, T.-P. (2018) Magmatic-hydrothermal evolution of the Donggou porphyry Mo deposit at the southern margin of the North China Craton: Evidence from chemistry of biotite. Ore Geology Reviews, 92, 84–96, https://doi.org/10.1016/j.oregeorev.2017.10.026.
Jin, X.-Y., Hofstra, A.H., Hunt, A.G., Liu, J.-Z., Yang, W., and Li, J.-W. (2020) Noble gases fingerprint the source and evolution of ore-forming fluids of carlin-type gold deposits in the golden triangle, south China. Economic Geology and the Bulletin of the Society of Economic Geologists, 115, 455–469, https://doi.org/10.5382/econgeo.4703.
Jochum, K.P., Weis, U.W., Stoll, B., Kuzmin, D., Yang, Q., Raczek, I., Jacob, D.E., Stracke, A., Birbaum, K., Frick, D.A., and others. (2011) Determination of reference values for NIST SRM 610–617 glasses following ISO guidelines. Geostandards and Geoanalytical Research, 35, 397–429, https://doi.org/10.1111/j.1751-908X.2011.00120.x.
John, D.A. (2001) Miocene and early Pliocene epithermal gold-silver deposits in the northern Great Basin, western USA—Characteristics, distribution, and relationship to magmatism. Economic Geology and the Bulletin of the Society of Economic Geologists, 96, 1827–1853, https://doi.org/10.2113/gsecongeo.96.8.1827.
John, D.A. and Henry, C.D. (2020) Magmatic-tectonic settings of Cenozoic epithermal gold-silver deposits of the Great Basin, western United States. In F.R. Koutz and W.M. Pennell, Eds., Vision for Discovery, Geological Society of Nevada 2020 Symposium Proceedings, Reno, p. 765–796. Geological Society of Nevada.
John, D.A., Henry, C.D., and Colgan, J.P. (2008) Magmatic and tectonic evolution of the Caetano caldera, north-central Nevada: A tilted, mid-Tertiary eruptive center and source of the Caetano Tuff. Geosphere, 4, 75–106, https://doi.org/10.1130/GES00116.1.
Johnson, C.L. (2020) The relationship between Eocene magmatism and gold mineralization in the Great Basin, USA: Insights from the Phoenix-Fortitude porphyry-skarn system and regional intrusions associated with mineralization, 485 p. Ph.D. thesis, University of Nevada.
Johnson, C.L., Dilles, J.H., Kent, A.J.R., Farmer, L.P., Henry, C.D., and Ressel, M.W. (2015) Petrology and geochemistry of the Emigrant Pass volcanics, Nevada: Implications for a magmatic-hydrothermal origin of the Carlin gold deposits. In W.M. Pennell and L.J. Garside, Eds., Proceedings of the Geological Society of Nevada, New Concepts and Discoveries Symposium, Reno/Sparks, Nevada, Extended Abstract, 391–408. Geological Society of Nevada.
Johnson, C.L., Ressel, M.W., and Ruprecht, P. (2020) Toward a global Carlin-type exploration model: The relationship between Eocene magmatism and diverse gold-rich deposits in the Great Basin, USA. Vision for discovery. Geology and Ore Deposits of the Basin and Range, 1, 355–382.
Jones Crafford, A.E.J. (2008) Paleozoic tectonic domains of Nevada: An interpretive discussion to accompany the geologic map of Nevada. Geosphere, 4, 260–291, https://doi.org/10.1130/GES00108.1.
Kamenetsky, V.S. and Danyushevsky, L. (2005) Metals in quartz-hosted melt inclusions: Natural facts and experimental artifacts. American Mineralogist, 90, 1674–1678, https://doi.org/10.2138/am.2005.1969.
Kularatne, K. and Audétat, A. (2014) Rutile solubility in hydrous rhyolite melts at 750–900 °C and 2 kbar, with application to titanium-in-quartz (TitaniQ) thermobarometry. Geochimica et Cosmochimica Acta, 125, 196–209, https://doi.org/10.1016/j.gca.2013.10.020.
Large, R.R., Bull, S.W., and Maslennikov, V. (2011) A carbonaceous sedimentary source-rock model for Carlin-type and orogenic gold deposits. Economic Geology and the Bulletin of the Society of Economic Geologists, 106, 331–358, https://doi.org/10.2113/econgeo.106.3.331.
Large, S.J.E., Bakker, E.Y.N., Weis, P., Wälle, M., Heinrich, C.A., and Ressel, M.W. (2016) Trace elements in fluid inclusions of sediment-hosted gold deposits indicate a magmatic-hydrothermal origin of the Carlin ore trend. Geology, 44, 1015–1018, https://doi.org/10.1130/G38351.1.
Le Maitre, R.W. (1989) A Classification of Igneous Rocks and Glossary Of Terms: Recommendations of the IUGS Subcommission of the Systematics of Igneous Rocks, 193 p. Blackwell.
Lee, S.-Y., Barnes, C.G., Snoke, A.W., Howard, K.A., and Frost, C.D. (2003) Petrogenesis of Mesozoic, peraluminous granites in the Lamoille Canyon area, Ruby Mountains, Nevada, USA. Journal of Petrology, 44, 713–732, https://doi.org/10.1093/petrology/44.4.713.
Lehmann, B. (1982) Metallogeny of tin; magmatic differentiation versus geochemical heritage. Economic Geology and the Bulletin of the Society of Economic Geologists, 77, 50–59, https://doi.org/10.2113/gsecongeo.77.1.50.
Liu, Y., Zhang, Y., and Behrens, H. (2005) Solubility of H2O in rhyolitic melts at low pressures and a new empirical model for mixed H_2O–CO_2 solubility in rhyolitic melts. Journal of Volcanology and Geothermal Research, 143, 219–235, https://doi.org/10.1016/j.jvolgeores.2004.09.019.
Loucks, R.R. (2021) Deep entrapment of buoyant magmas by orogenic tectonic stress: Its role in producing continental crust, adakites, and porphyry copper deposits. Earth-Science Reviews, 220, 103744, https://doi.org/10.1016/j.earscirev.2021.103744.
Lowenstern, J.B. (2015) Bursting the bubble of melt inclusions. American Mineralogist, 100, 672–673, https://doi.org/10.2138/am-2015-5254.
Ludington, S. and Plumlee, G.S. (2009) Climax-type porphyry molybdenum deposits. U.S. Geological Survey Open-File Report, Volume 2009–1215.
Mahood, G. and Hildreth, W. (1983) Large partition coefficients for trace elements in high-silica rhyolites. Geochimica et Cosmochimica Acta, 47, 11–30, https://doi.org/10.1016/0016-7037(83)90087-X.
McDonough, W.F. and Sun, S.-S. (1995) The composition of the Earth. Chemical Geology, 120, 223–253, https://doi.org/10.1016/0009-2541(94)00140-4.
McQuarrie, N. and Oskin, M. (2010) Palinspastic restoration of NAVDat and implications for the origin of magmatism in southwestern North America. Journal of Geophysical Research: Solid Earth, 115, 1–16.
Mercer, C.N. (2021) Eocene magma plumbing system beneath Cortez Hills Carlin-type gold deposit, Nevada: Is there a deep-seated pluton? Economic Geology and the Bulletin of the Society of Economic Geologists, 116, 501–513, https://doi.org/10.5382/econgeo.4821.
Mercer, C.N. and Hofstra, A.H. (2020) Melt inclusion and mineral geochemical analyses supporting the evaluation of petrogenesis, degassing, and metallogenic potential of mid-Cenozoic rhyolite magmas in northern Nevada, USA (Version 2.0, March 2025). U.S. Geological Survey Data Release, https://doi.org/10.5066/P9UWAW28.
Mercer, C.N., Hofstra, A.H., Todorov, T.I., Roberge, J., Burgisser, A., Adams, D.T., and Cosca, M. (2015) Pre-eruptive conditions of the Hideaway Park topaz rhyolite: Insights into metal source and evolution of magma parental to the Henderson porphyry molybdenum deposit, Colorado. Journal of Petrology, 56, 645–679, https://doi.org/10.1093/petrology/egv010.
Moore, L.R., Gazel, E., Tuohy, R., Lloyd, A.S., Esposito, R., Steele-MacInnis, M., Hauri, E.H., Wallace, P.J., Plank, T., and Bodnar, R.J. (2015) Bubbles matter: An assessment of the contribution of vapor bubbles to melt inclusion volatile budgets. American Mineralogist, 100, 806–823, https://doi.org/10.2138/am-2015-5036.
Morgan, G.B. and London, D. (1996) Optimizing the electron microprobe analysis of hydrous alkali aluminosilicate glasses. American Mineralogist, 81, 1176–1185, https://doi.org/10.2138/am-1996-9-1016.
Mortensen, J.K., Thompson, J.P.H., and Tosdal, R.M. (2000) U-Pb age constraints on magmatism and mineralization in the northern Great basin. Proceedings of the Geological Society of Nevada, Reno/Sparks, Nevada, Extended Abstracts, 61–65.
Munoz, J.L. (1984) F-OH and Cl-OH exchange in micas with applications to hydrothermal ore deposits. Reviews in Mineralogy and Geochemistry, 13, 469–494.
Muntean, J.L. (2018) The Carlin gold system: Applications to exploration in Nevada and beyond. In J.L. Muntean, Ed., Diversity in Carlin-Style Gold Deposits. Reviews in Economic Geology, Vol. 20, p. 39–88. Society of Economic Geologist.
Muntean, J.L. and Cline, J.S. (2018) Introduction: Diversity in Carlin-Style Gold Deposits. In J.L. Muntean, Ed., Diversity in Carlin-Style Gold Deposits. Reviews in Economic Geology, Vol. 20, p. 1–5. Society of Economic Geologists.
Muntean, J.L., Cline, J.S., Simon, A.C., and Longo, A.A. (2011) Magmatic-hydrothermal origin of Nevada's Carlin-type gold deposits. Nature Geoscience, 4, 122–127, https://doi.org/10.1038/ngeo1064.
Myers, M.L., Wallace, P.J., Wilson, C.J.N., Morter, B.K., and Swallow, E.J. (2016) Prolonged ascent and episodic venting of discrete magma batches at the onset of the Huckleberry Ridge supereruption, Yellowstone. Earth and Planetary Science Letters, 451, 285–297, https://doi.org/10.1016/j.epsl.2016.07.023.
Myers, M.L., Wallace, P.J., and Wilson, C.J.N. (2019) Inferring magma ascent timescales and reconstructing conduit processes in explosive rhyolitic eruptions using diffusive losses of hydrogen from melt inclusions. Journal of Volcanology and Geothermal Research, 369, 95–112, https://doi.org/10.1016/j.jvolgeores.2018.11.009.
Neukampf, J., Ellis, B.S., Magna, T., Laurent, O., and Bachmann, O. (2019) Partitioning and isotopic fractionation of lithium in mineral phases of hot, dry rhyolites: The case of the Mesa Falls Tuff, Yellowstone. Chemical Geology, 506, 175–186, https://doi.org/10.1016/j.chemgeo.2018.12.031.
Newman, S. and Lowenstern, J.B. (2002) VolatileCalc: A silicate melt–H_2O–CO_2 solution model written in Visual Basic for Excel. Computers & Geosciences, 28, 597–604, https://doi.org/10.1016/S0098-3004(01)00081-4.
Norling, B., Rowe, M.C., Chambefort, I., Tepley, F.J. III, and Morrow, S. (2016) Volatile behavior and trace metal transport in the magmatic–geothermal system at Pūtauaki (Mt. Edgecumbe), New Zealand. Journal of Volcanology and Geothermal Research, 318, 27–44, https://doi.org/10.1016/j.jvolgeores.2016.02.010.
Nutt, C.J. (2000) Geologic map of the Alligator Ridge area, including the Buck Mountain East and Mooney Basin Summit quadrangles and parts of the Sunshine Well NE and Long Valley Slough quadrangles, White Pine County, Nevada. U.S. Geological Survey, Geologic Investigations Series I-2691.
Nutt, C.J. and Hofstra, A.H. (2003) Alligator Ridge District, East-Central Nevada: Carlin-type gold mineralization at shallow depths. Economic Geology and the Bulletin of the Society of Economic Geologists, 98, 1225–1241, https://doi.org/10.2113/gsecongeo.98.6.1225.
Olson, N.H. (2022) Petrologic investigations into the magmatic processes that lead to Au, Ag, and base metal fertility: Insights from Pebble, Alaska and the

Emigrant Pass Volcanic Field, Nevada, 325 p. Ph.D. thesis, Oregon State University.
Pearce, J.A., Harris, N.B.W., and Tindle, A.G. (1984) Trace element discrimination diagrams for the tectonic interpretation of granitic rocks. Journal of Petrology, 25, 956–983, https://doi.org/10.1093/petrology/25.4.956.
Ressel, M.W. and Henry, C.D. (2006) Igneous geology of the Carlin trend, Nevada: Development of the Eocene plutonic complex and significance for Carlin-type gold deposits. Economic Geology and the Bulletin of the Society of Economic Geologists, 101, 347–383, https://doi.org/10.2113/gsecongeo.101.2.347.
Ressel, M.W., Noble, D.C., Henry, C.D., and Trudel, W.S. (2000) Dike-Hosted Ores of the Beast Deposit and the Importance of Eocene Magmatism in Gold Mineralization of the Carlin Trend, Nevada. Economic Geology and the Bulletin of the Society of Economic Geologists, 95, 1417–1444, https://doi.org/10.2113/95.7.1417.
Richards, J.P. (2011) High Sr/Y arc magmas and porphyry Cu±Mo±Au deposits: Just add water. Economic Geology and the Bulletin of the Society of Economic Geologists, 106, 1075–1081, https://doi.org/10.2113/econgeo.106.7.1075.
Richards, J.P. and Kerrich, R. (2007) Special Paper: Adakite-like rocks. Their diverse origins and questionable role in metallogenesis. Economic Geology and the Bulletin of the Society of Economic Geologists, 102, 537–576, https://doi.org/10.2113/gsecongeo.102.4.537.
Richards, J.P., Spell, T., Rameh, E., Razique, A., and Fletcher, T. (2012) High Sr/Y magmas reflect arc maturity, high magmatic water content, and porphyry Cu ± Mo ± Au potential: Examples from the Tethyan arcs of central and eastern Iran and western Pakistan. Economic Geology and the Bulletin of the Society of Economic Geologists, 107, 295–332, https://doi.org/10.2113/econgeo.107.2.295.
Robb, L. (2020) Introduction to Ore-forming Processes, 2nd edition. Wiley-Blackwell.
Rose-Koga, E.F., Bouvier, A.S., Gaetani, G.A., Wallace, P.J., Allison, C.M., Andrys, J.A., Angeles de la Torre, C.A., Barth, A., Bodnar, R.J., Bracco Gartner, A.J.J., and others. (2021) Silicate melt inclusions in the new millennium: A review of recommended practices for preparation, analysis, and data presentation. Chemical Geology, 570, 120145, https://doi.org/10.1016/j.chemgeo.2021.120145.
Rosera, J., Frazer, R., Mills, R., Jacob, K., Gaynor, S., Coleman, D., and Farmer, G.L. (2023) Fluorine-Rich Mafic Lower Crust in The Southern Rocky Mountains: The Role of Pre-Enrichment in Generating Fluorine Rich Silicic Magmas and Porphyry Mo Deposits. American Mineralogist, 108, 1573–1596, https://doi.org/10.2138/am-2022-8503.
Rottier, B., Rezeau, H., Casanova, V., Kouzmanov, K., Moritz, R., Schlöglova, K., Wälle, M., and Fontboté, L. (2017) Trace element diffusion and incorporation in quartz during heating experiments. Contributions to Mineralogy and Petrology, 172, 23, https://doi.org/10.1007/s00410-017-1350-4.
Rottier, B., Kouzmanov, K., Ovtcharova, M., Ulianov, A., Wälle, M., Selby, D., and Fontboté, L. (2020) Multiple rejuvenation episodes of a silicic magma reservoir at the origin of the large diatreme-dome complex and porphyry-type mineralization events at Cerro de Pasco (Peru). Lithos, 376-377, 105766, https://doi.org/10.1016/j.lithos.2020.105766.
Rudnick, R.L. and Gao, S. (2014) 4.1–Composition of the continental crust. In H.D. Holland and K.K. Turekian, Eds., Treatise on Geochemistry, 2nd Edition, p. 1–51. Elsevier.
Ryskamp, E.B., Abbott, J.T., Christiansen, E.H., Keith, J.D., Vervoort, J.D., and Tingey, D.G. (2008) Age and petrogenesis of volcanic and intrusive rocks in the Sulphur Spring Range, central Nevada: Comparisons with ore-associated Eocene magma systems in the Great Basin. Geosphere, 4, 496–519, https://doi.org/10.1130/GES00113.1.
Schneider, C.A., Rasband, W.S., and Eliceiri, K.W. (2012) NIH Image to ImageJ: 25 years of image analysis. Nature Methods, 9, 671–675, https://doi.org/10.1038/nmeth.2089.
Sepp, M.D. (2022) What lies beneath? Origin and transition from the shallow epithermal Au-Ag lithocap to deeper porphyry Cu environment: Insights from the magmatic hydrothermal deposits at Yerington, Nevada, and Summitville, Colorado, 275 p. Ph.D. thesis, University of Oregon.
Severs, M.J., Azbej, T., Thomas, J.B., Mandeville, C.W., and Bodnar, R.J. (2007) Experimental determination of H_2O loss from melt inclusions during laboratory heating: Evidence from Raman spectroscopy. Chemical Geology, 237, 358–371, https://doi.org/10.1016/j.chemgeo.2006.07.008.
Seward, T., Williams-Jones, A., and Migdisov, A. (2014) Treatise on Geochemistry. Geochemistry of Mineral Deposits, 13, 29–57.
Shabani, A.A.T., Lalonde, A.E., and Whalen, J.B. (2003) Composition of biotite from granitic rocks of the Canadian Appalachian orogen: A potential tectonomagmatic indicator? Canadian Mineralogist, 41, 1381–1396, https://doi.org/10.2113/gscanmin.41.6.1381.
Sinclair, W.D. (1995) Porphyry Mo (Climax-type): in Selected British Columbia mineral deposit profiles. In D.V. Lefebure and G.E. Ray, Eds., Metallics and coal, British Columbia Ministry of Energy of Employment and Investment Open File 1995–20, 105–108.
Sisson, T.W. and Grove, T.L. (1993) Experimental investigations of the role of H2O in calc-alkaline differentiation and subduction zone magmatism. Contributions to Mineralogy and Petrology, 113, 143–166, https://doi.org/10.1007/BF00283225.
Skjerlie, K.P. and Johnston, A.D. (1992) Vapor-absent melting at 10 kbar of a biotite- and amphibole-bearing tonalitic gneiss: Implications for the generation of A-type granites. Geology, 20, 263–266, https://doi.org/10.1130/0091-7613(1992)020<0263:VAMAKO>2.3.CO;2.
Smith, M.T., Rhys, D., Ross, K., Lee, C., and Gray, J.N. (2013) The Long Canyon deposit: Anatomy of a new off-trend sedimentary rock-hosted gold discovery in northeastern Nevada. Economic Geology and the Bulletin of the Society of Economic Geologists, 108, 1119–1145, https://doi.org/10.2113/econgeo.108.5.1119.
Snee, J.-E.L. and Miller, E.L. (2022) Magmatism, migrating topography, and the transition from Sevier shortening to Basin and Range extension, western United States. In J.P. Craddock, D.H. Malone, B.Z. Foreman, and A. Konstantinou, Eds., Tectonic Evolution of the Sevier-Laramide Hinterland, Thrust Belt, and Foreland, and Postorogenic Slab Rollback (180–20 Ma). The Geological Society of America.
Sparks, R.S.J., Annen, C., Blundy, J.D., Cashman, K.V., Rust, A.C., and Jackson, M.D. (2019) Formation and dynamics of magma reservoirs. Philosophical Transactions. Series A, Mathematical, Physical, and Engineering Sciences, 377, 20180019, https://doi.org/10.1098/rsta.2018.0019.
Thorkelson, D.J. and Breitsprecher, K. (2005) Partial melting of slab window margins: Genesis of adakitic and non-adakitic magmas. Lithos, 79, 25–41, https://doi.org/10.1016/j.lithos.2004.04.049.
Timmermans, A.C., Cousens, B.L., and Henry, C.D. (2020) Geochemical study of Cenozoic mafic volcanism in the west-central Great Basin, western Nevada, and the Ancestral Cascades Arc, California. Geosphere, 16, 1179–1207, https://doi.org/10.1130/GES01535.1.
Tosdal, R.M., Wooden, J.L., and Kistler, R.W. (2000) Geometry of the Neoproterozoic continental break-up, and implications for location of Nevadan mineral belts. In J.K. Cluer, J.G. Price, E.M. Struhsacker, R.F. Hardyman, and C.L. Morris, Eds., Proceedings of the Geological Society of Nevada, Geology and Ore Deposits 2000: The Great Basin and Beyond. Reno, 451–466.
Tretbar, D.R., Arehart, G.B., and Christensen, J.N. (2000) Dating gold deposition in a Carlin-type gold deposit using Rb/Sr methods on the mineral galkhaite. Geology, 28, 947–950, https://doi.org/10.1130/0091-7613(2000)28<947:DGDIAC>2.0.CO;2.
Vigneresse, J.L. (1995) Crustal regime of deformation and ascent of granitic magma. Tectonophysics, 249, 187–202, https://doi.org/10.1016/0040-1951(95)00005-8.
Vikre, P.G., Poulson, S.R., and Koenig, A.E. (2011) Derivation of S and Pb in Phanerozoic intrusion-related metal deposits from Neoproterozoic sedimentary pyrite, Great Basin, United States. Economic Geology and the Bulletin of the Society of Economic Geologists, 106, 883–912, https://doi.org/10.2113/econgeo.106.5.883.
Vikre, P., John, D., Wintzer, N.E., Koutz, F., Graybeal, F., Dail, C., and Annis, D.C. (2023) Critical minerals in subduction-related magmatic-hydrothermal systems of the United States. U.S. Geological Survey Scientific Investigations Report 2023–5082.
Walker, J.A., Teipel, A.P., Ryan, J.G., and Syracuse, E. (2009) Light elements and Li isotopes across the northern portion of the Central American subduction zone. Geochemistry, Geophysics, Geosystems, 10, 6, https://doi.org/10.1029/2009GC002414.
Wallace, P.J. and Edmonds, M. (2011) The sulfur budget in magmas: Evidence from melt inclusions, submarine glasses, and volcanic gas emissions. Reviews in Mineralogy and Geochemistry, 73, 215–246, https://doi.org/10.2138/rmg.2011.73.8.
Watson, E.B. and Harrison, T.M. (1983) Zircon saturation revisited: Temperature and composition effects in a variety of crustal magma types. Earth and Planetary Science Letters, 64, 295–304, https://doi.org/10.1016/0012-821X(83)90211-X.
Watts, K.E., John, D.A., Colgan, J.P., Henry, C.D., Bindeman, I.N., and Schmitt, A.K. (2016) Probing the volcanic–plutonic connection and the genesis of crystal-rich rhyolite in a deeply dissected supervolcano in the Nevada Great Basin: Source of the late Eocene Caetano Tuff. Journal of Petrology, 57, 1599–1644, https://doi.org/10.1093/petrology/egw051.
Watts, K.E., John, D.A., Colgan, J.P., Henry, C.D., Bindeman, I.N., and Valley, J.W. (2019) Oxygen isotopic investigation of silicic magmatism in the Stillwater caldera complex, Nevada: Generation of large-volume, low-$\delta^{18}O$ rhyolitic tuffs and assessment of their regional context in the Great Basin of the western United States. Geological Society of America Bulletin, 131, 1133–1156, https://doi.org/10.1130/B35021.1.
Webster, J.D., Holloway, J.R., and Hervig, R.L. (1987) Phase equilibria of a Be, U and F-enriched vitrophyre from Spor Mountain, Utah. Geochimica et Cosmochimica Acta, 51, 389–402, https://doi.org/10.1016/0016-7037(87)90057-3.
Wones, D.R. (1989) Significance of the assemblage titanite+ magnetite+ quartz in granitic rocks. American Mineralogist, 74, 744–749.
Wones, D.R. and Eugster, H.P. (1965) Stability of biotite: Experiment, theory, and application. American Mineralogist, 50, 1228–1272.
Xue, Q., Zhang, L., Chen, S., Guo, K., Li, T., Han, Z., and Sun, W. (2023) Tracing black shales in the source of a porphyry Mo deposit using molybdenum isotopes. Geology, 51, 688–692, https://doi.org/10.1130/G51240.1.

Yonkee, W.A. and Weil, A.B. (2015) Tectonic evolution of the Sevier and Laramide belts within the North American Cordillera orogenic system. Earth-Science Reviews, 150, 531–593, https://doi.org/10.1016/j.earscirev.2015.08.001.

Zajacz, Z., Hanley, J.J., Heinrich, C.A., Halter, W.E., and Guillong, M. (2009) Diffusive reequilibration of quartz-hosted silicate melt and fluid inclusions: Are all metal concentrations unmodified? Geochimica et Cosmochimica Acta, 73, 3013–3027, https://doi.org/10.1016/j.gca.2009.02.023.

Zen, E.A. (1988) Phase relations of peraluminous granitic rocks and their petrogenetic implications. Annual Review of Earth and Planetary Sciences, 16, 21–51, https://doi.org/10.1146/annurev.ea.16.050188.000321.

Zhang, D. and Audétat, A. (2017) Chemistry, Mineralogy and Crystallization Conditions of Porphyry Mo-forming Magmas at Urad–Henderson and Silver Creek, Colorado, USA. Journal of Petrology, 58, 277–296, https://doi.org/10.1093/petrology/egx016.

Zhang, W., Lentz, D.R., Thorne, K.G., and McFarlane, C. (2016) Geochemical characteristics of biotite from felsic intrusive rocks around the Sisson Brook W-Mo-Cu deposit, west-central New Brunswick: An indicator of halogen and oxygen fugacity of magmatic systems. Ore Geology Reviews, 77, 82–96, https://doi.org/10.1016/j.oregeorev.2016.02.004.

Zhang, C., Li, X., Almeev, R.R., Horn, I., Behrens, H., and Holtz, F. (2020) Ti-in-quartz thermobarometry and TiO2 solubility in rhyolitic melts: New experiments and parametrization. Earth and Planetary Science Letters, 538, 116213, https://doi.org/10.1016/j.epsl.2020.116213.

Manuscript received February 27, 2024
Manuscript accepted May 4, 2025
Accepted manuscript online May 15, 2025
Manuscript Handled by Antonio Acosta-Vigil

Endnotes:

[1]Deposit item AM-25-129372. Online Materials are free to all readers. Go online, via the table of contents or article view, and find the tab or link for supplemental materials.